Rapid assembly of a polar network architecture by formins downstream of RhoA pulses drives efficient cortical actomyosin contractility

Vlad Costache[1,*], Serena Prigent Garcia[1,*], Camille N. Plancke[1], Jing Li[2], Simon Begnaud[1], Shashi Kumar Suman[1], Taeyoon Kim[2], François B. Robin[1,✉]

1: CNRS UMR7622 and Inserm ERL 1156, Institute for Biology Paris-Seine (IBPS), Sorbonne University, Paris, France.
2: Weldon School of Biomedical Engineering, Purdue University, West Lafayette, Indiana.

*: Contributed equally
✉: Corresponding author. Email: francois.robin@sorbonne-universite.fr

SUMMARY

Actin network architecture and dynamics play a central role in cell contractility and tissue morphogenesis. Pulsed contractions driven by RhoA represent a generic mode of actomyosin contractility, but the mechanisms underlying how their specific architecture emerges and how this architecture supports network contractility remain unclear. Here, we combine quantitative microscopy, single-molecule imaging, numerical simulations and simple mathematical modelling, to explore the dynamical network architecture underlying pulsed contraction. We first describe two subpopulations of formins that are recruited from the cytoplasm and bind to the cell surface in the early *C. elegans* embryo: activated formins, a functionally inactive population, and active formins, which actively participate in Actin network assembly. Focusing on formin dynamics during pulses, we show that activated formins precede and largely outnumber active formins, a kinetic assembly scheme compatible with formins capturing and rapidly saturating free barbed ends available for filament elongation. We then show that these active formins assemble a polar network of actin, with barbed ends pointing out of the pulse, and our numerical simulations demonstrate that this geometry favors rapid network contraction. Our results thus show that formins convert the RhoA biochemical gradient caused by RhoA pulses in a polar network architecture, while saturating available actin filaments barbed ends, thereby driving rapid and effective network contractility, an important evolutionary feature in a metazoan with a rapid embryonic cell cycles.

HIGHLIGHTS

1. CYK-1 drives actin network assembly during pulses
2. The process is extremely rapid, with a formin-based actin elongation rate higher than 1.3 $\mu m \cdot s^{-1}$
3. A barbed-end saturation mechanism allows for effective and responsive F-actin assembly
4. Rapid and responsive F-actin elongation results in assembly of aster-like polar actin networks
5. Numerical simulations show network polarity drives very efficient network contractility

INTRODUCTION

Vastly conserved in eukaryotes, the actomyosin cytoskeleton is a major determinant of the mechanical properties of embryonic cells and tissues (Munjal & Lecuit 2014). Modulation of the activity of actomyosin networks plays a critical role in cell shape changes, cell division, cell migration and polarization, and the integration of these behaviors, at the tissue scale, drive tissue deformation and morphogenesis (Lecuit & Lenne 2007). Meanwhile, the role of the architecture of actomyosin networks has been a research focus and subject to some debate. In muscle, the mechanisms for actomyosin contractility has been historically well-characterized, showing that in this quasi-crystalline organization, the sliding of bipolar Myosin II mini-filaments along actin filaments drives network contractility. In other cell types however, and in particular in the cell cortex of developing embryos, actin network organization remains poorly understood in terms of network polarity, length distribution, mesh size, turnover rates or crosslinking levels, and we still do not fully understand how F-actin architecture is linked to network contractility. Theoretical studies (Galkin et al. 2010; Galkin et al. 2011; Lenz, Gardel, et al. 2012) and computational models (T. Kim 2015) have shown that asymmetry between compressive and extensive modulus can drive contraction of disordered bundles. Similarly, numerical simulations (Yu et al. 2018) and *in vitro* experiments have clearly demonstrated that non-polar actin networks can contract. Cellular networks however often display characteristic organizations, suggesting that specific network dynamics and geometries may play a critical role in network contractility (Koenderink & Paluch 2018).

RhoGTPases zones have recently emerged as essential regulators to template the remodeling of the actomyosin meshwork (Benink 2005; Miller & Bement 2009; Burkel et al. 2012; Bement et al. 2005) to define active, task-tuned zones of cytoskeletal assembly and remodeling.. Examples of such zones include the leading edge of migrating cells, the cleavage furrow during cell division, or the apical cortex during apical constriction. During embryonic morphogenesis in particular, a wide class of morphogenetic processes are driven by brief iterative contractions of the cortical actomyosin network termed pulsed contractions (He et al. 2010; H. Y. Kim & Davidson 2011; Martin et al. 2009; Munro et al. 2004; Roh-Johnson et al. 2012). Previous work showed that pulsed contractions are driven by excitable dynamics of the Rho GTPase RhoA, leading to the formation of activation zones that drive the recruitment of downstream effectors formin, Anillin, F-actin and Myosin II (Maddox et al. 2005; Munro et al. 2004; Michaux, Robin, McFadden & Munro 2018a; Naganathan et al. 2018; Reymann et al. 2016). Excitable dynamics seem to play an important role to establish Rho activation(Bement et al. 2015; Maître et al. 2015; Nishikawa et al. 2017; Michaux, Robin, McFadden & Munro 2018b).

It remains unclear, however, how the upstream RhoGTPases spatially and temporally orchestrate the recruitment, turnover, activity of their downstream effectors to support the cellular function of these Rho zones. Here, we show that the dynamics and topology of RhoA activation, converting a RhoA chemical

gradient into the assembly of a polar actin network, drives the formation of a network structure tuned to its contractile function.

In the nematode *C. elegans*, pulsed contractions occur from the 1-cell stage onwards during interphase (Munro et al. 2004) and support cell polarization and apical constriction (Nance & Priess 2002; Nance 2003; Roh-Johnson et al. 2012). Here, we show that RhoA driven network assembly (Michaux, Robin, McFadden & Munro 2018a; Naganathan et al. 2018) controls the accumulation of the formin CYK-1 (diaphanous/mDia homolog), driving F-actin accumulation during pulsed contractions. Combining our results on formin-based actin elongation rates with F-actin turn-over rates (Robin et al. 2014; Michaux, Robin, McFadden & Munro 2018a), we show that formins elongate filaments with an exponential length distribution and with mean length of ~6 μm. We further show that actin network assembly is kinetically controlled by the saturation of actin filaments barbed ends, resulting in a time-optimal response to RhoA activation. Fast formin elongation with saturating kinetics allows for a fast and effective assembly of actin networks. Using single-molecule microscopy to measure actin filament orientation during pulse assembly, we show that actin networks by CYK-1 assembled are polar, generating networks with barbed ends pointing outside of the pulse. Finally, our computational exploration shows that this polar network architecture is favorable to the generation of effective actomyosin contractility.

Actomyosin network contractility is a key conserved feature of eukaryotic cells. For example, yeast nodes (Vavylonis et al. 2008) and *C. elegans* pulses (Munro et al. 2004) bear striking biochemical resemblances: composed of the same basic ingredients (formins, assembling long actin filaments ; Myosin II motors driving network contractility by pulling on the actin cables), their assembly is also under the control of RhoGTPases. The geometry of nodes and pulses, however, is opposite to one-another. In yeast, the *Search-Capture-Pull-Release* model proposes that actin filament barbed ends are associated with nodes/asters, pointed ends pointing away from the node (Pollard & Wu 2010; Vavylonis et al. 2008). Here, we show that in *C. elegans* actomyosin pulses assemble a dynamic architecture, in which actin filaments barbed ends transiently point out of the node, in a striking dissimilarity with yeast.

Taken together, these results underline a kinetic rather than mechanical control for actomyosin network orientation during pulsed contractions. They also underline the tinkering evolution of billion-years old machinery, reusing the molecular machines –formin, F-actin and Myosin II– to drive a fundamentally conserved phenomenon –precisely-tuned force generation– with opposite geometries reflecting organism-specific construction rules and constraints.

RESULTS

CYK-1::GFP elongates actin filaments extremely fast

Formins are actin nucleators and processive actin elongators, catalyzing the addition of actin monomers to the barbed end of actin filaments while protecting the filament against capping (Pruyne et al. 2002). In *C. elegans*, 7 formin genes have been identified (Mi-Mi et al. 2012). Among these, *cyk-1* (cytokinetic defective-1), the only ortholog of the Diaphanous family of formins, is required for cell division (Swan et al. 1998).

To measure the activity of CYK-1 in the early *C. elegans* embryos, we used live single-molecule fluorescence microscopy to visualize the dynamics of individual formin molecules fused with GFP (Robin et al. 2014). We first observed that formins apparently classified in at least two populations (Movie S1a and S1b), a population of ballistic molecules and a static population. To better visualize these two populations, we used maximum intensity projection to overlay the position of molecules over 100 consecutive time-points (Movie S2a and S2b). Using this visualization tool, static formins appeared as dots, while moving formins appeared as a trail on the cell surface.

To quantitatively characterize these two populations, we performed single-particle tracking and analyzed the trajectories of 19137 individual formin molecules from 5 embryos. Based on the logarithmic regression of the mean-squared displacement to an anomalous diffusion model $MSD = 2*D.t^{\alpha}$ (Robin et al. 2014), we characterized all particle trajectories longer than 15 frames (Fig. 1A,B) by their anomalous diffusion coefficient D and scaling exponent α. Strikingly, we observed the emergence of two clear populations, corresponding to the ballistic and static populations, with apparent distributions of scaling exponent peaking at $\alpha = 0.3$ (subdiffusive) and $\alpha = 1.6$ (superdiffusive), respectively (Fig. 1C,D, Movie S3).

Previous works suggested that these ballistic particles represented formins actively elongating actin filaments (Higashida 2004; Funk et al. 2019). In order to verify that these super-diffusive particles indeed reflected actin-elongating filaments, we used worms fed with RNAi against *perm-1*, which codes for a known component eggshell protein (Carvalho et al. 2011; Olson et al. 2012) to permeabilize the eggshell, and subsequently treated the embryos with the microtubule depolymerizing drug Nocodazole and the actin depolymerizing drug Latrunculin A (Movie S4a-b and S5). Performing the same analysis as previously, we observed that the superdiffusive population essentially disappeared after Latrunculin A treatment, while it was unaffected by Nocodazole treatment (Fig. 1E, Movie S5). These results strongly supported the idea that superdiffusive cortical CYK-1::GFP speckles corresponded to formin dimers actively and processively elongating actin filaments at the barbed-end of the filament at the cell cortex.

To measure the speed of formins, we selected a collection of trajectories projected formin motion on a smoothed version of their trajectory, and quantified the traveled distance along this trajectory, or using MSD measurements presented before. Both metrics, quite conservative, yielded very similar result of $1.1 \pm 0.2\ \mu m \cdot s^{-1}$ and $1.3 \pm 0.2\ \mu m \cdot s^{-1}$ (standard deviation) – in line with previously reported speeds (Higashida 2004), but slower than recent *in vivo* reports (Funk et al. 2019). Interestingly, single-molecule

microscopy of actin::GFP (Movie S11, (Robin et al. 2014)) did not display similar directional motion, suggesting that actin filament elongation fully translates in CYK-1 directional motion. These data show that CYK-1 velocity is a reliable *in vivo* proxy for formins elongation rate, demonstrating an average elongation rate of ~400–468 monomers·s^{-1}. Incidentally, our results thus suggest that CYK-1 could be used as a biosensor to measure cellular modulations of the concentrations of profilin-ATP-G-Actin, calibrated on elongation rates previously reported *in vitro* in the presence of profilin (Neidt, Scott, et al. 2008; Neidt, Skau, et al. 2008). Provided that in our system formin elongation rates are not buffered by slow dissociation of profilin from the barbed end (Funk et al. 2019), our results here would point to a local G-actin concentration in the early embryo is in the ~10-12 μM range.

Formin dynamics during the cell cycle

To explore if actin elongation was dynamically modulated during embryonic development, we then measured formin velocity at the 1-, 2- and 4-cell stages during distinct phases of the cell cycle (Fig. 2A, see Material and Methods). At the 1-cell stage, elongation rate remained unchanged from polarization to maintenance phase (1.25 ± 0.18 μm·s^{-1} and 1.27 ± 0.16 μm·s^{-1}, resp.), but decreased significantly during cytokinesis to 1.05 ± 0.22 μm·s^{-1}.

The velocity increased again after cytokinesis, going back to its level at corresponding 1-cell stage polarization establishment (1.24 ± 0.19 μm·s^{-1}), stable or slightly decreasing during mitosis (1.18 ± 0.18 μm·s^{-1}) in the AB cell, to drop down again during AB cytokinesis (1.04 ± 0.18 μm·s^{-1}). Again, during interphase at the 4-cell stage in ABp, formin velocity increased again though notably lower at interphase than at mitosis (1.15 ± 0.17 μm·s^{-1} at interphase and 1.24 ± 0.18 μm·s^{-1} during mitosis). This result suggests that the system takes longer to recover the formin speed as the development goes but maintains a very constant speed during cytokinesis and interphase, the period of speed recovery occurring at interphase.

To compare actin elongation rates across lineages, we also measured the formin speed in AB (1.24 ± 0.19 μm·s^{-1}) and P1 (1.18 ± 0.18 μm·s^{-1}) at the 2-cell stage during interphase, and also during mitosis (1.18 ± 0.18 μm·s^{-1} and 1.22 ± 0.19 μm·s^{-1} resp.) (Fig. 2B). Our results show that the formin speed does not seem to vary between the two cell types.

In summary, actin elongation dynamics is distinctly modulated during phases of the cell cycle, decreasing significantly by >10% during cytokinesis, to increase again after cytokinesis completion. Strikingly, measured elongation rates seemed relatively robust and only changed marginally from the 1-cell to 4-cell stage. These results suggest that F-actin dynamics might be differentially regulated by G-actin concentration, but remains largely robust across cell lineages during early embryonic development.

Formin kinetics and implications on actin filament length *in vivo*

The length of formin-elongated filaments is controlled by a combination of the elongation rate of formins and the turnover rate of F-actin monomers in the cortex. Specifically, we assumed that F-actin turnover and formin elongation are independent processes and follow exponential laws with characteristic rate $\lambda_1 = 1/\tau_1$ and $\lambda_2 = 1/\tau_2$. For an F-actin monomer being disassembled, the length of filament to the barbed-end of the filament follows an exponential law with characteristic rate $V_f \times \lambda_{12}$ with $\lambda_{12} = \lambda_1 + \lambda_2$ (see Suppl. Material for detailed derivation). To estimate filament length, we thus needed to access τ_2 and τ_2, in addition to formin speed.

We expected a significant fraction of trajectory to be interrupted, either by tracking failure or photobleaching, barring us from using single-molecule tracking as a proxy (Fig. S1B,C). We therefore turned to a previously established strategy, smPReSS (Robin et al. 2014) to estimate a bulk turnover rate for formins. By measuring the depletion of cortical formins caused by laser illumination of the cortex in a CYK-1 overexpression strain, we could establish that the bulk cortical turnover rate of CYK-1 is ~0.11 s^{-1} (Fig. S1D).

Combining these results with previous measurements of Actin::GFP turnover rates (Robin et al. 2014; Michaux, Robin, McFadden & Munro 2018a) we estimate that formin elongated filaments scale to ~6 μm on average at the 2-cell stage in the early *C. elegans* embryo.

Dynamics of formin recruitment at the cortex during pulsed contractions

We then decided to focus on the dynamics of formin during pulsed contractions. During polarity establishment in the 1-cell embryo, and during S-phase at the 2-cell stage, formins accumulate in well-identifiable pulses corresponding to actomyosin pulsed contractions (Fig. S1A, Movie S2a-b, S14a). To infer the biochemical sequence of formin activation during pulsed contractions, we thus decided to measure the timing of arrival of the various formin populations over the course of a pulsed contraction.

As described previously, in order to categorize into subdiffusive or superdiffusive, a minimal track length was required. We thus divided the population into 3 tiers: short tracks (<15 consecutive time frames), which could not be categorized into a specific population, long subdiffusive and long superdiffusive. Using this technique, we were able to demonstrate that the ratio between the different populations was finely modulated during pulses (Fig. 3A-C, E-F). To characterize the dynamics of arrival of these populations at the cell cortex, we first focused on the kinetics of recruitment on a sequence of individual pulses (Fig. 3A-C). Strikingly, we observed an iterated sequence of recruitment. Using cross-correlation, we measured a delay between the arrival of the superdiffusive and subdiffusive populations of ~2.7 s (Fig. 3D). This suggested that the distinct populations were recruited in a sequence at the cortex, superdiffusive formins (hereon, "active" formins) accumulating first, followed by subdiffusive formins (hereon "activated" formins).

To confirm this result, we collected a series of 116 CYK-1 pulses from , and averaged the arrival of the distinct populations. Based on these results, we observed that formins were indeed recruited to the cortex in a well-defined sequence, starting with superdiffusive followed by subdiffusive formins. We further confirmed this observation using a different metrics based directly on particle displacements instead of trajectory classification to measure this delay (Fig. S3A-F), and yielding very similar delays (Fig. S3G,H).

This result was somewhat surprising, as based on previous works on formin structure and domain activity, we expected an activation sequence whereby formins would be first recruited to the cortex by Rho, then transferred to barbed-ends of actin filaments to promote elongation (Li & Higgs 2005; Higgs 2005; Li & Higgs 2003). Numerically however, the number of recruited formins far out-weighted the elongating population, suggesting that the system might be running in a regime in which formins are in excess, and elongate a limiting pool of barbed ends available for elongation.

A barbed end saturation mechanism allows for responsive actin assembly

To test this hypothesis, we designed a simple kinetic model for CYK-1 recruitment, and used this model to explore the temporal dynamics of formin accumulation. We assumed that:

(1) RhoA activation activity is smooth and periodic,

(2) inactive formins are activated by RhoA and recruited to the cortex, shifting in the **"activated"** population,

(3) CYK-1 formins are poor nucleators but good elongators – we considered that formins do not efficiently nucleate new filaments under physiological conditions (*in vitro* actin assembly yields ~1 new nucleated filament per 550 CYK-1 formin molecule at 2.5 μM actin and 2.5 μM profilin PFN-1 (Neidt, Skau, et al. 2008)),

(4) once recruited at the cortex, formins bind to barbed ends through a bimolecular reaction to drive actin assembly, becoming **"active"**,

(5) activated formins unbind from the cortex, returning back to the cytoplasmic pool,

(6) active formins unbind from the cortex to the cytoplasmic pool.

To seed our model, we used known values for the model regarding formin turnover rates and RhoA activity and relative ratios between the different populations. Using these parameters, we could recapitulate our key observation that active formins accumulated before inactive formins under the condition that (1) the binding reaction of activated formins to barbed ends is very fast and (2) barbed ends are scarce and are depleted when formin density increases (Fig. 4A-C). Under these conditions, during an early phase active formins accumulate rapidly following the RhoA pulse, followed by a late phase during which the accumulation of activated formins (Fig. 4B,I, Fig. S4A).

We favored a model for activation in which RhoA binding preceded dimerization (Fig. S4B), though other models with the dimer pre-existing Rho binding and formin unfolding should not be excluded. The simulation however proved robust to these modifications of the biochemical scheme (Fig. 4G,H).

These results show that given a small set of assumptions, we could explain the emergence of a significant delay between "activated" and "active" formins. This model suggests that the saturation by CYK-1 of the barbed-ends of actin filament allows for a rapid response to pulsed RhoA activation (Fig. 4D-F). This suggests that the kinetics of the actin cytoskeleton in the early *C. elegans* embryo is wired to drive fast response to an upstream activation of actin dynamics.

Relative rates of actin assembly and contractility support polar network assembly

During pulsed contractions, cortical contractile dynamics results in peak flow rates of ~0.3 $\mu m \cdot s^{-1}$ (Michaux, Robin, McFadden & Munro 2018a; Munro et al. 2004; Nishikawa et al. 2017). In comparison, formin elongation rates are relatively rapid, with a measured speed of 1.1 – 1.3 $\mu m \cdot s^{-1}$. As a consequence, even at the peak of contraction, formins can "exit" the contraction zone easily and assemble an actin network of filaments up to several microns around the pulse region. To describe the architecture of this network, we measured the orientation of formin-based actin elongation during pulse assembly. To this end, we focused on **active** formins, and measured the orientation of elongation radially away from the zone of formin accumulate (Fig. 5A-C), which essentially corresponds to the RhoA recruitment zone (Fig. S2). Displaying only orientations where we could collect >200 individual elongation measurements, we observed that while formins are not heavily oriented outside of the pulse time-window (Fig. 5D,E). In contrast, during the peak of assembly (approx. corresponding to the period where >50% max active formins are recruited), formins displayed a strong polarization (Fig. 5D).

These results show that formins elongate the actin network with a polar dynamics, elongation during the pulse occurring from the center of the pulse to the outside. As formin-based elongation increases local actin concentration ~2-fold, we propose that pulses assemble a polar actin network with barbed-ends pointing outwards of the pulse akin to an "actin aster" (Fig. 7C,D).

To test if this orientation resulted purely from the transient local gradient of active formins between the pulsing region and its surroundings, or if additional mechanisms should be invoked, we designed a simple spatial model of formin orientation. To seed our model, we exclusively used measured parameters of formin recruitment and elongation dynamics (formin elongation rate, density, activation duration, and off-rate, and pulsed contractions localizations), and generated synthetic formin pulsed accumulations with random orientations. Modelled formin elongation dynamics displayed similar orientations, with filaments pointing outwards, and closely mirroring the dynamics observed *in vivo* (Fig. S5, Movie S6). Altogether, these results demonstrate that local formin accumulation drives the assembly of a polar actin network architecture with a majority of barbed ends pointing out.

While previous work, both theoretical (Lenz, Thoresen, et al. 2012; Lenz, Gardel, et al. 2012) and *in vitro* (Linsmeier et al. 2016), showed that actin contraction does not require a specific network orientation, *in vivo* observations (Coravos & Martin 2016) suggested that pulsed contractions form a polar actin network. Strikingly, recent *in vitro* and computational work show that Myosin II contractility can drive polar network reorganization by barbed end filament sorting, with an opposite polarity (Kreten et al. 2018; Wollrab et al. 2018). We thus wondered if the polar network architecture we observed, barbed end pointing out, would not support either stronger contractions or contraction over larger distances. However, we realized that controlling independently network orientation and density, while constraining other parameters *in vivo* or *in vitro* would not be possible. We thus decided to turn to agent-based models of cortical mechanics to test the impact of network architecture on contractility.

Network polarity is adapted to effective and rapid contractility

Using our established computational model of the actomyosin networks (Jung et al. 2015; Bidone et al. 2017; T. Kim 2015) (Fig. S7A), we probed the roles of formin-induced F-actin elongation in cortex mechanics and architecture. Using a cortex-like, 20 μm wide and 100 nm thick, actin meshwork, we simulated pulsed contraction by locally modulating the kinetics of Myosin II and F-actin elongation rates, based on experimental measurements (Fig. S7B). Specifically, to reproduce formin activity, we immediately increased the elongation rate of a fraction of the barbed ends in the activated region, resulting in rapid elongation of actin filaments up to ~12 μm for ~10 s (Fig. 6A, top row). 5 s after actin elongation onset, we then locally turned on Myosin II activity in the activated region for 15 s to reproduce delayed Myosin II activation by RhoA.

Using the model, we evaluated how formin activation affects network structures and the deployment of forces generated by Myosin II in the cortex. As expected, we found that actin and myosin tended to contract toward the center of the activated region upon motor activation (Fig. 6B and S7C). Interestingly, the maximum levels of actomyosin contraction were inversely proportional to formin activation level (Fig. 6B and S7D). We observed that formin-elongated actin filaments experienced large tensile forces during the contraction of actin filaments and myosin motors (Fig. 6A, second row and S7D). This implies that those long actin filaments are cross-linked with many other short actin filaments, propagating the force generated by myosin farther in the network. The sum of tensile forces acting on these elongated filaments was proportional to the fraction of formin-elongated filaments (Fig. S7E). When more actin filaments were elongated by formin, the resistance to contraction became stronger, thus inhibiting local collapse of the network and enabling force transmission farther in the cortex.

We also focused on actin aggregates formed during pulsed contractions. Weaker local contraction and long-ranged force transmission in the network prevented the formation of contraction-induced actin aggregates

separated from the rest of the network (Fig. 6A-B). However, if formin activation is too high, myosin and actin contraction were both inhibited (Fig. 6B, S7E, Movie S10).

In order to explore the specific role of network polarity, we probed the mechanics of network with opposite architecture, by artificially enhancing polymerization at pointed ends. Interestingly, we observed that myosin concentration was enhanced, but actin contraction was weakened, compared to the case with enhanced polymerization at barbed ends (Fig. 6D, E). Tensile forces acting along the formin-elongated filaments also reduced (Fig. 6G). These results reflect the fact that, in this architecture, myosin motors merely move toward the pulse center, in a polarity sorting mechanism (Fig. 6D), rather than pulling actin filaments to develop forces.

DISCUSSION

Precise architectural organization of the actomyosin network is crucial for force generation at the cell cortex. How such architectures are assembled in a dynamic network with fast turnover stands as a multiple answer question during development where force deployment is critical for embryo morphogenesis. Here, we show that formins organize a polar actin network during cortical pulsed contraction, in a biochemical system primed for rapid assembly.

Our results are based on a detailed description of the kinetics of actin assembly by formins. We show that formins elongate actin filaments at 1.2 $\mu m \cdot s^{-1}$, or ~450 $monomers \cdot s^{-1}$. Formin elongation in vitro has been proposed to overcome diffusion limiting rates (Drenckhahn & Pollard 1986), likely by allowing formins to "explore" a larger volume to "find" monomers (Courtemanche 2018). Assuming that elongation rates scale with the concentration of actin, in a solvent-independent manner (that is, independently of viscosity – affecting the diffusion rate, or crowding effects, where solutes in the cell do not affect elongation rates of CYK-1), then formin velocity provides a good indicator of the modulations of free G-actin concentration in the cell. Recent work has shown that under saturating conditions, at concentrations of actin > 200 μM, the formin elongation rate can increase experimentally up to ~1200 $monomers \cdot s^{-1}$ (Funk et al. 2019). Furthermore, a replacement of the FH1 and FH2 domains of the formins indicated that the FH2 domain, rather than FH1, was responsible for setting the specific maximal elongation rate. Strikingly, *in vivo* elongation rates were also measured to be close to their maximal *in vitro* velocity for the considered formins (~1450 $monomers \cdot s^{-1}$ for mDia2 and 860 $monomers \cdot s^{-1}$ for mDia1, in a manner robust to variations in G-Actin and profilin concentration (Funk et al. 2019)).

Our analyses revealed that, within tracks longer than 250ms (5 frames) – the only ones where a robust mobility analysis can be performed – two distinct populations with specific mobilities are recruited at the cell surface: superdiffusive and subdiffusive formins. We attributed these populations to active and activated formins populations, respectively. Upon binding with RhoA, cytoplasmic formins would unfold and bind

to the cell surface, then diffuse in the vicinity on the inner face of the plasma membrane to find an available barbed-end to bind and elongate that filament. Kinetically, therefore, we expected the activation sequence to read (1) **inactive**, then (2) **activated**, and finally (3) **active**. The observed kinetic sequence we observed however was (1) inactive, then (2) active, then (3) activated but inactive. To explore how this dynamics could emerge, we developed a biochemical model to see if we could reconciliate our biochemical scheme with our observations. Our model showed that the two models come together under a specific set of assumptions where barbed ends available for elongation are limiting, formins are recruited in large numbers and the conversion reaction is fast compared to other reactions in the system. Our results therefore suggest that the actin in *C. elegans* is biochemically primed for rapid response. When the RhoA signaling cascade is activated, actin assembly is saturated by formins, with an over-crowding of formins to drive an efficient and optimally rapid response to signaling cues.

Strikingly, the set of assumptions we designed seems robust to variations in the biochemical activation scheme used, as it was sufficient to recover the described dynamics under a variety of models (Fig. 4G,H). Recycling of the formins after elongation had stopped seemed to complicate the recovery the observed dynamics. And while our approach does not exclude other possible models – for example an accumulation of cortical formins after an initial period of elongation – the observed kinetics of collections of individual trajectories did substantiate these alternative models.

While the analysis of CYK-1 dynamics provides a new and interesting perspective on the dynamics of barbed ends at the cortex during activation by RhoA, we still lack tools to conclusively explore a collection of issues: when are barbed ends generated and by which mechanisms (Myosin II driven filament severing; formin-based nucleation?), what is the dynamics of capping during pulses, how many barbed ends are generated? We also do not have yet the resolution to explore the specific nature of the observed barbed ends: are formins capable of hetero-dimerizing, and could this yield to the formation of inactive barbed ends, these other formins acting as competitive inhibitors for CYK-1 elongation?

In this context, the activation of RhoA pulses drives rapid actin assembly. Strikingly, the geometry of the assembled network is controlled by the geometry of the upstream signaling factors: local RhoA activation drives the assembly of a polar actin network. The geometry of the assembled structure is well tuned for actomyosin contractility, with Myosin II recruited at the center of the prospective pulsed contraction, while actin is assembled in a polar aster network, with barbed ends pointing outwards of the assembled architecture. Our numerical simulations show that, while actomyosin networks can generate tension in the absence of a specific network architecture, actomyosin networks perform differently depending on their organization and the contractile efficiency of actomyosin network remains functionally linked to their geometry. Therefore, the actin assembly transduction machinery downstream of RhoA converts a chemical RhoA gradient into a polar actin network architecture, with a structure well adapted to the contractile function of actomyosin pulses in morphogenesis.

With precisely timed cell cycles, similar in duration to the ones in Drosophila syncytial embryo, lasting ~10', *C. elegans* embryonic early development cell cycles unfold very fast (Brauchle et al. 2003) – compared to other early embryos, for instance in mouse embryos early cell cycles last about 20 h (Yamagata & FitzHarris 2013), sea urchin 150 min (Chassé et al. 2016) or even ascidians (~30 min) (Dumollard et al. 2013). In *C. elegans*, the 10 min cycles are divide roughly equally, into ~5 min for mitosis and 5 min interphase with cortical pulses. As a consequence, cell polarity, compartmentalization, and cell shape changes are heavily constrained in time. An actin network primed for fast assembly, together with the polar architecture of actomyosin pulsed contractions, may set the stage for rapid and efficient contractions and cell shape changes. During gastrulation, this very same organization may thus drive a fast apical constriction, and a subsequent timely internalization of endodermal cells.

Strikingly, the contractile structure assembled in *C. elegans* is very similar in its biochemical composition to the nodes assembled in fission yeast during contractile ring assembly: formin filament elongators, Myosin II motors and actin cables. However, several key differences separate the two contractile modules. Structurally, the size of the biological systems diverge strongly. At the level of the cell, a fission yeast cell spans ~14 µm long and 3 µm wide during cell division, against 50 µm in length and 30 µm in width for the *C. elegans* embryo (Fig 7A,B). The two contractile macromolecular assemblies are also very different: fission yeast nodes are <600nm wide and initially distant by <1 µm on average, while *C. elegans* actomyosin pulses are 5 µm wide and separated by 5-10µm. The two systems are also biochemically distinct. The fission yeast formin Cdc12p elongates actin filaments with high processivity (k_{off} ~7.10^{-5} s^{-1}) but slow speed (10.6 monomers·s^{-1} at 1.5 µM [Actin], 4 µM [SpPRF], fission yeast profilin), while the *C. elegans* formin CYK-1 elongates actin filaments with a lower processivity (k_{off} ~4.10^{-3} s^{-1}) but much higher speed (63.2 monomers·s^{-1} at 1.5 µM [Actin] and 4 µM [PFN-1], the *C. elegans* profilin). In the *Search-Pull-Capture-Release* model, actin filament elongation takes place from a static barbed end (Pollard & Wu 2010; Vavylonis et al. 2008). However, in *C. elegans*, a similar mechanism would result in filament buckling or stalling in actin filament elongation. To drive the same functional output – contraction – the molecular homologs assemble a structurally distinct (geometrically opposite) architecture which is tuned to the scale of the biological system, revealing here an interesting instance of the tinkering of evolution.

ACKNOWLEDGEMENTS

We thank Anne-Cecile Reymann, Stephan Grill, Ronen Zaidel-Bar and Geraldine Seydoux for worm strains, and express in particular our gratitude to Anne-Cécile Reymann for sharing the CYK-1::GFP overexpression strain in 2013. We thank Marie Breau for manuscript revisions, Michel Labouesse, Marie Breau and members of the Labouesse laboratory for valuable discussions, as well as members of the Robin laboratory for discussions and technical assistance.

This work was supported by the ATIP/Avenir and ERC-Tremplin programs (to F.B. Robin).
The authors declare no competing financial interests.

MATERIAL AND METHODS

***C. elegans* culture and strains.**

We cultured *C. elegans* strains under standard conditions (Brenner 1974). We used the following *C. elegans* strains: CYK-1::GFP over-expression (Reymann et al. 2016) ; CYK-1::GFP CRISPR, FBR160 ; NMY2::GFP x Lifeact:: mKate2, SWG007 ; CYK-1::GFP x NMY2::GFP ; CYK-1::GFP overexp x Lifeact::mKate ; CYK-1::GFP CRISPR x Lifeact::mKate ; CYK-1::mNeon CRISPR ; GFP::actin, JH1541, unc-119(ed4); pJH7.03 [unc-119; pie-1::GFP::actin::pie-1 3' UTR] (courtesy of G. Seydoux) ; GFP::utrophin, MG589, mgSi3[Cb-unc-119(+) pie-1::GFP::utrophin::pie-1 3' UTR] II (3);

RNA interference.

We performed RNAi using the feeding method as previously described (Timmons & Fire 1998). Bacteria targeting Perm-1 and GFP were obtained from the Kamath feeding library (Kamath et al. 2003).

The L4417 plasmid targeting Perm-1 or the entire GFP sequence (generated by the Fire lab and available at http://www.addgene.org/1649/) was transformed into HT115(DE3) bacteria. Bacterial cultures for feeding were grown for 10–12 h and then induced on standard nematode nutritional growth media plates containing 50 µg/ml ampicillin and 1 mM IPTG for 16–24 h at 20–25 °C, then stored at 4 °C. For Perm-1 RNAi, L4 stage larvae were placed on feeding plates for 16–24 h before imaging.

Imaging conditions.

We dissected gravid hermaphrodites and mounted one-cell embryos under #1.5 22-mm square coverslips in 2.5 µl of MiliQ water or standard Egg Salts buffer (118 mM NaCl, 40 mM KCl, 3.4 mM CaCl2, 3.4 mM MgCl2, 5 mM HEPES, pH 7.4) containing ~500 uniformly sized polystyrene beads (15.6 ± 0.03 µm diameter, Bangs labs, #NT29N) to achieve uniform compression of the embryo surface across experiments (Robin et al. 2014).

We performed near-TIRF imaging at 19–21°C on an inverted Nikon Ti-E N-Storm microscope, equipped with motorized TIRF illuminator, Apo TIRF 100x Oil-immersion DIC N2 objective (Nikon) with 1.49–numerical aperture (NA), and PFS-S Perfect Focus unit (Nikon). Laser illumination at 488 nm and 561 nm from 300 mW solid-state sapphire laser (Coherent) was set at 30 % of maximal power and delivered by fiber optics to the TIRF illuminator. Images were magnified by a 1.5× lens and collected on an Andor iXon Ultra DU-897 EMCCD camera, yielding a pixel size of 107 nm.

We controlled laser illumination angle and intensity and image acquisition using NIS Elements software (Nikon). For all experiments, we set the laser illumination angle to a standard value that was chosen empirically to approximately maximize signal intensity while maintaining even illumination across the field of view. For all SPT experiments, we collected images in streaming mode with continuous illumination at 15–60% laser intensity (100% ≈ 1.6 $\mu W \cdot \mu m^{-2}$) with 50 ms exposures to achieve frame rates of 20 frames/s.

Tuning GFP levels to achieve single-molecule densities

The quasi-steady-state densities observed during imaging depend on the initial (unobserved) densities, photobleaching rates and the intrinsic exchange kinetics of the target molecule (see main text and below). We thus determined the appropriate initial densities empirically for a given strain and experiment. We achieved these initial densities by using two methods as previously described (Robin et al. 2014). For GFP overexpression strains, we used RNAi directed against the GFP sequence to deplete the pool of GFP-tagged proteins. RNAi against maternal proteins typically yields an exponential decrease in the maternal protein with time of exposure (Oegema & Hyman 2006). We controlled the degree of depletion by synchronizing larvae and sampling embryos at different times after the initiation of feeding to identify times at which discrete diffraction-limited speckles were observed at the cell surface. The optimal time was relatively consistent across experiments for a given strain and varied from 12–36 h depending on transgene expression levels and relative abundance at the cell surface vs. cytoplasm. To fine-tune density levels, we used brief (<10 s) pulses in epi-illumination mode at high laser power until adequate density was reached (Robin et al. 2014).

Drug perfusion experiments

For exposing embryos to 10 μM of Latrunculin A (Sigma L5163) or to 10 μg/mL of Nocodazole (Sigma M1404) in Egg Salts buffer during image acquisition, we used wider coverslips (22 mm x 30 mm) so that a perfusion chamber is formed between coverslip and slide, and the coverslip passes about 3 mm from the side of the slide. On the inverted microscope, this outer side of coverslip helps as support to able to deposit the perfusion volume as a drop (4 μL) while imaging, The drug solution likewise perfused by capillarity between slide and coverslip exposes the embryos to the drug instantly. A bright field (BF) illumination marks this moment on the acquired movie for downstream image analysis.

Assessing potential effects of compression, laser exposure and GFP tagging.

We followed experimental procedures as previously tested (Robin et al. 2014). Using photobleaching to reduce GFP-tagged protein levels from full to single-molecule levels in one step resulted in arrested development. However, the laser exposure required to fine-tune densities by photobleaching, or that occurring during single-molecule imaging, did not cause embryos to arrest. In all of our single-molecule imaging experiments, we verified that embryos initiated and completed cytokinesis with normal timing or, in the case of nocodazole treated embryos multiple nuclei were present in the cell.

Single-molecule detection and tracking.

We used a publicly available Matlab implementation of the Crocker-Grier algorithm for single-particle detection and tracking (Pelletier et al. 2009; Crocker & Grier 1996). In brief, the Crocker-Grier method localizes particles to subpixel resolution in individual frames by fitting local intensity peaks to a Gaussian point spread function. The two key detection parameters—peak and mean intensity of the candidate particles—are adjusted empirically for given imaging conditions using a graphical user interface. The particles are then linked frame to frame by minimizing the global displacement across all particles, given a user-chosen cutoff value for maximum particle displacement. A second parameter, the gap size, allows the possibility of ignoring 'gaps' in a trajectory due to transient failures to detect particles. These transient failures occur mainly because motion blur causes the particle intensity to fall transiently below the detection threshold.

To estimate actin concentration, we assumed that elongation rates scale linearly with actin concentration, and used previously measured elongation rates of 60 monomers$\cdot s^{-1}$,at 1.5 μM ATP-Actin (Neidt, Scott, et al. 2008; Neidt, Skau, et al. 2008).

To infer filament length, we made the following assumptions:

1. actin monomers display simple mono-exponential half-life at the cortex,
2. actin monomers display a half-life measured by tracking and smPReSS of 0.08-0.15 s (Robin et al. 2014; Michaux, Robin, McFadden & Munro 2018a),
3. active formins display simple mono-exponential half-life at the filament barbed end,
4. active formins display a half-life measured by smPReSS of ~0.11 s.

Under these assumptions, we consider solely actin filaments assembled by formins. From the perspective of an actin monomer at the time of disassembly, two options are possible:

(1) the monomer disassembles while the formin is still elongating,

(2) the formin unbinds and elongation stops before the monomer disassembles.

The "effective" elongation time of the formin on the filament is then the minimum value between (1) and (2). If actin lifetime and formin elongation time have independent exponential distributions of parameters $\lambda_1 = 1/\tau_1$ and $\lambda_2 = 1/\tau_2$, then the minimum between the two values also has exponential distribution of parameter $\lambda_{12} = 1/\tau_{12} = 1/\tau_1 + 1/\tau_2$. Under these conditions, the length of the elongated filament then is:

$$L_{filament} = V_{elongation} \times \tau_{12} = \frac{V_{elongation}}{\frac{1}{\tau_1} + \frac{1}{\tau_2}}$$

Formin Speed measurement analysis

We performed single-molecule imaging as described previously. We mounted the embryos between glass slides with squares wells of 20 μm thick Epoxy and #1.5 coverslips (170 μm thick) in 2.5 μL of filtered MilliQ water with 15.4 μm polystyrene beads. We imaged single molecules using 50% of 90mW of 488 nm laser, 50 ms of exposure, no delay between frames, using Photometrics 95B prime 22 mm sCMOS camera. Laser angle was set to 65°. Room temperature set up between 19 and 20.5°C. After acquisition, we averaged

two consecutive frames, in order to achieve 10 frames per second using ImageJ software (NIH Image, Bethesda, MD). We used Matlab implementation of the Crocker-Grier algorithm ((Crocker & Grier 1996)) by the Kilfoil lab for single-particle tracking. The following parameters were used: particle size, 2 pixels, maximal displacement of the particle between two consecutive frames, 3.5 pixels and the memory to link trajectories in non-consecutive frames, 0 frame. We selected manually a ROI to exclude tracks from residual particles outside the cell for each stage: whole embryo for one-cell stage, anterior (AB) cell for two-cell stage, posterior AB daughter cell (ABp) for four-cell stage. Each stage has been separated into three steps corresponding to the cell cycle: interphase (corresponding to the phase where pulsed contractions can be seen at the cortex), mitosis (where the pulsed contractions have stopped) and cytokinesis (when the cleavage furrow can be seen).

Subsequent image analysis was performed in Matlab through a pipeline. We selected the trajectories based on their anomalous diffusion coefficient D and scaling exponents α. Tracks were classified in subdiffusives and superdiffusives accordingly and only the latter were kept. Tracks can have multiple behaviors during their lifetime (switchs between sub- and superdiffusive) (Movie S13), in order to calculate the velocity only during elongation of actin filaments a second selection was made to keep tracks with only superdiffusive behavior (Movie S12). Manual checking of plots of the tracks was used to keep the tracks that were closer to a line, in order to have the best approximation of the particle speed. To measure the speed of the formin we calculate the displacement between first frame and last frame divided by the number of frames required for this movement by the time step of 100 ms.

Statistical analysis

23 to 40 tracks per embryo were selected. Normal distributions were verified. Two-sample Student tests (t-tests) were performed to measure the significance of the difference in speed between each stage and phase. *** means $p<0.001$, ** means $p<0.01$, ns: non-significant.

Two-color imaging microscopy

We performed single-molecule imaging as described previously. Acquisitions were performed with the Andor iXon 897 EMCCD camera. We imaged at 30% of 90 mW for 488 nm and 561 nm, 50 ms exposure (e.g. 100 ms between two frames of the same color), no delay between frames. After acquisition, we averaged five consecutive frames, in order to achieve 2 frames per second using ImageJ. Pulsed contractions were selected manually and data from the intensity profile of a line drawn through the pulse is collected in a single frame. 3 pulses per embryo in 6 embryos (total of 18) were analysed in Matlab (R2018a version). Intensities are smoothened and normalized with maximum being 1 and immediately preceding minimum being 0. Data for myosin (NMY-2::mKate, in red channel) is aligned at 0,98% of the maximum and this alignment is propagated to the corresponding data in the green channel (domain derived from C-terminus of Anillin fused to a GFP used as a sensor for active RhoA, AHPH::GFP ; or CYK-1::GFP for formin).

Tracking of individual pulses of CYK-1::GFP

We used a semi-automatic approach to identify and follow CYK-1 pulses during the two-cell stage interphase, in the anterior blastomere. We manually identified isolated pulses and drew a ROI over the surface of each pulse (about 6 μm in diameter), at about 5 frames before maximum contraction of the area can be detected. The ROI was then automatically propagated in time before and after t0, and also we designed a Matlab script (Fig. S6) allowing to adapt automatically the surface of the ROI in order to include the full trajectory of particles appearing within the ROI. To eliminate cortical drift of the ROI du to the full contractility of the cortex, independently of CYK-1 displacement within the pulse area, we used a mean correction of the displacement of each tracked particle, if the neighboring particles were having exactly the same displacement. This was important for the mobility classification of particles in superdiffusive or subdiffusive; in order not to add artificial directional movement, du to displacement of the full cortical area where the CYK-1 particle was present.

Single particles tracking and pulse analysis pipeline in Matlab

We designed an analysis pipeline based on Matlab scripts (Fig. S6, code available upon request) that includes CYK-1::GFP particles detection and tracking, reduction to the surface of the embryo and the AB cell, dedrifting of the trajectories and MSD analysis for segregation in different mobility populations (mainly superdiffusive CYK-1 vs. subdiffusive CYK-1). The further step is to intersect the matrix of all these trajectories with the specific ROI of each pulse. The final step is to normalize and align all the pulses (number of particles in time) with respect to their maximum and the minimum number of particles before, then to measure the angle orientation of every vector formed by the trajectories with respect to the center of the ROI.

Numerical simulation of formin local recruitment

We used MATLAB to compute a 2D simulation of local formin activation and actin elongation. Pulses were spatially and temporally distributed in an embryo's shaped mask in a random manner. Pulse were defined by a fixed 5x5 μm window (100x100 pixels) and a 20 seconds time window (400 frames). Pulses could not overlap in time and space. Using experimental data, density of formin recruitment, position around the pulse center and kinetics of recruitment could be computed in each pulse. We added 0.01 formins recruitment /μm^2/frame all over the embryo mask (independent of pulses generation) corresponding to the formin recruitment rate observed in areas away from a pulse. According to experimental data, 80% of the formin recruited were assigned to be subdiffusive while 20% of them were assigned superdiffusive. Since we aimed to study superdiffusive particles, we approximate sub-diffusive and diffusive particles as a unique population of immobile particles. Each position of superdiffusive tracks were computed using the following sequence. The length of the step R_n was picked in a normal distribution whose mean is 1.2286 μm/s and standard deviation is 0.2950 μm/s (values extracted from experimental data). The orientation θ_n of the step was calculated assuming a persistent length P_L of 15μm (close to the actin persistence length, (Howard 2001)).

$$\theta_{n+1} = \theta_n + X \times \arccos\left(e^{-\frac{R}{2 \cdot P_L}}\right),\ with\ X \sim \mathcal{N}(0,1)$$

Length of track were assigned using the distribution of track length for sub-diffusive and super-diffusive particles, respectively. Simulated data were analyzed using the same methods as experimental data.

Model overview

For simulations in this study, we used a well-established agent-based model of actomyosin networks based on the Langevin equation [1-4]. The detailed descriptions about the model and all parameters used in the model are explained in Supplementary Text and Table S1. In the model, actin filament (F-actin), motor, and ACP are coarse-grained using cylindrical segments (Fig. S7a). The motions of all the cylindrical segments are governed by the Langevin equation for Brownian dynamics. Deterministic forces in the Langevin equation include bending and extensional forces that maintain equilibrium angles formed by segments and the equilibrium lengths of segments, respectively, as well as a repulsive force acting between neighboring pairs of segments for considering volume-exclusion effects.

The formation of F-actin is initiated by a nucleation event, followed by polymerization at the barbed end and depolymerization at the pointed end. ACPs bind to F-actin without preference for cross-linking angles at a constant rate and also unbind from F-actin at a force-dependent rate determined by Bell's law [5]. Each arm of motors binds to F-actin at a constant rate, and it then walks toward the barbed end of F-actin or unbinds from F-actin at force-dependent rates determined by the parallel cluster model [6, 7]. For all simulations in this study, we used a thin computational domain (20×20×0.1 μm) with periodic boundary conditions only in x and y directions (Fig. S7b). In z direction, the boundaries of the domain exert repulsive forces on elements that moved beyond the boundaries. At the beginning of each simulation, a thin actin network is formed via self-assembly of F-actin and ACP.

For implementing rho activation, the domain is divided into 16 subdomains (4×4 in x and y directions). Every 30 s, one of the subdomains is randomly selected and then activated. In the activated subdomain, a fraction of the barbed ends of F-actins are randomly chosen and then undergo faster polymerization by a factor, ϱ_f, for the duration of τ_f. With the reference values of $\varrho_f = 10$ and $\tau_f = 10$ s, F-actins are elongated by ~10 μm on average. After the time delay of d_M, motors in the activated subdomain are allowed to self-assemble into thick filament structures for the duration of τ_M. The reference values of d_M and τ_M are 5 s and 15 s, respectively. These active motors in the form of thick filaments can contract the part of the network in the activated subdomain. Once they become inactive after τ_M, the motors are disassembled into monomers that cannot bind to F-actin.

BIBLIOGRAPHY

Bement, W.M. et al., 2015. Activator-inhibitor coupling between Rho signalling and actin assembly makes the cell cortex an excitable medium. *Nature Cell Biology*, 17(11), pp.1471–1483.

Bement, W.M., Benink, H.A. & Dassow, von, G., 2005. A microtubule-dependent zone of active RhoA during cleavage plane specification. *The Journal of Cell Biology*, 170(1), pp.91–101.

Benink, H.A., 2005. Concentric zones of active RhoA and Cdc42 around single cell wounds. *The Journal of Cell Biology*, 168(3), pp.429–439.

Bidone, T.C. et al., 2017. Morphological Transformation and Force Generation of Active Cytoskeletal Networks. A. R. Asthagiri, ed. *PLoS computational biology*, 13(1), p.e1005277.

Brauchle, M., Baumer, K. & Gönczy, P., 2003. Differential activation of the DNA replication checkpoint contributes to asynchrony of cell division in C. elegans embryos. *Current Biology*, 13(10), pp.819–827.

Brenner, S., 1974. The Genetics of CAENORHABDITIS ELEGANS. *Genetics*, 77(1), pp.71–94.

Burkel, B.M. et al., 2012. A Rho GTPase signal treadmill backs a contractile array. *Developmental Cell*, 23(2), pp.384–396.

Carvalho, A. et al., 2011. Acute drug treatment in the early C. elegans embryo. B. Lehner, ed. *PLoS ONE*, 6(9), p.e24656.

Chassé, H. et al., 2016. Cyclin B Translation Depends on mTOR Activity after Fertilization in Sea Urchin Embryos. *PLoS ONE*, 11(3), p.e0150318.

Coravos, J.S. & Martin, A.C., 2016. Apical Sarcomere-like Actomyosin Contracts Nonmuscle Drosophila Epithelial Cells. *Developmental Cell*, 39(3), pp.346–358.

Courtemanche, N., 2018. Mechanisms of formin-mediated actin assembly and dynamics. *Biophysical Reviews*, 10(6), pp.1553–1569.

Crocker, J.C. & Grier, D.G., 1996. Methods of digital video microscopy for colloidal studies. *Journal of Colloid and Interface Science*, 179(1), pp.298–310.

Drenckhahn, D. & Pollard, T.D., 1986. Elongation of actin filaments is a diffusion-limited reaction at the barbed end and is accelerated by inert macromolecules. *The Journal of biological chemistry*, 261(27), pp.12754–12758. Available at: https://pubmed.ncbi.nlm.nih.gov/3745211/.

Dumollard, R. et al., 2013. Beta-catenin patterns the cell cycle during maternal-to-zygotic transition in urochordate embryos. *Developmental Biology*, 384(2), pp.331–342.

Funk, J. et al., 2019. Profilin and formin constitute a pacemaker system for robust actin filament growth. *eLife*, 8, p.1826.

Galkin, V.E. et al., 2011. Remodeling of actin filaments by ADF/cofilin proteins. *Proceedings of the National Academy of Sciences of the United States of America*, 108(51), pp.20568–20572.

Galkin, V.E. et al., 2010. Structural polymorphism in Factin. *Nature Publishing Group*, 17(11), pp.1318–1323.

He, L. et al., 2010. Tissue elongation requires oscillating contractions of a basal actomyosin network. *Nature Cell Biology*, 12(12), pp.1133–1142. Available at: http://www.nature.com/doifinder/10.1038/ncb2124.

Higashida, C., 2004. Actin Polymerization-Driven Molecular Movement of mDia1 in Living Cells. *Science*, 303(5666), pp.2007–2010.

Higgs, H.N., 2005. Formin proteins: a domain-based approach. *Trends in biochemical sciences*, 30(6), pp.342–353.

Howard, J., 2001. *Mechanics of motor proteins and the cytoskeleton* Sinauer, ed.,

Jung, W., Murrell, M.P. & Kim, T., 2015. F-actin cross-linking enhances the stability of force generation in disordered actomyosin networks. 2(4), pp.317–327. Available at: https://link.springer.com/article/10.1007/s40571-015-0052-9.

Kamath, R.S. et al., 2003. Systematic functional analysis of the Caenorhabditis elegans genome using RNAi. *Nature*, 421(6920), pp.231–237.

Kim, H.Y. & Davidson, L.A., 2011. Punctuated actin contractions during convergent extension and their permissive regulation by the non-canonical Wnt-signaling pathway. *Journal of Cell Science*, 124(4), pp.635–646.

Kim, T., 2015. Determinants of contractile forces generated in disorganized actomyosin bundles. *Biomechanics and Modeling in Mechanobiology*, 14(2), pp.345–355.

Koenderink, G.H. & Paluch, E.K., 2018. Architecture shapes contractility in actomyosin networks. *Current Opinion in Cell Biology*, 50, pp.79–85.

Kreten, F.H. et al., 2018. Active bundles of polar and bipolar filaments. *Physical Review E*, 98(1-1), p.012413.

Lecuit, T. & Lenne, P.-F., 2007. Cell surface mechanics and the control of cell shape, tissue patterns and morphogenesis. *Nature Reviews Molecular Cell Biology*, 8(8), pp.633–644.

Lenz, M., Gardel, M.L. & Dinner, A.R., 2012. Requirements for contractility in disordered cytoskeletal bundles. *New Journal of Physics*, 14(3), p.033037.

Lenz, M., Thoresen, T., et al., 2012. Contractile Units in Disordered Actomyosin Bundles Arise from F-Actin Buckling. *Physical Review Letters*, 108(23), p.238107.

Li, F. & Higgs, H.N., 2005. Dissecting requirements for auto-inhibition of actin nucleation by the formin, mDia1. *The Journal of biological chemistry*, 280(8), pp.6986–6992.

Li, F. & Higgs, H.N., 2003. The mouse Formin mDia1 is a potent actin nucleation factor regulated by autoinhibition. *Current Biology*, 13(15), pp.1335–1340.

Linsmeier, I. et al., 2016. Disordered actomyosin networks are sufficient to produce cooperative and telescopic contractility. *Nature Communications*, 7, p.12615.

Maddox, A.S. et al., 2005. Distinct roles for two C. elegans anillins in the gonad and early embryo. *Development*, 132(12), pp.2837–2848.

Maître, J.-L. et al., 2015. Pulsatile cell-autonomous contractility drives compaction in the mouse embryo. *Nature Cell Biology*, 17(7), pp.849–855.

Martin, A.C., Kaschube, M. & Wieschaus, E.F., 2009. Pulsed contractions of an actin-myosin network drive apical constriction. *Nature*, 457(7228), pp.495–499. Available at: http://www.nature.com/doifinder/10.1038/nature07522.

Mi-Mi, L. et al., 2012. Z-line formins promote contractile lattice growth and maintenance in striated muscles of C. elegans. *The Journal of Cell Biology*, 198(1), pp.87–102.

Michaux, J.B., Robin, F.B., McFadden, W.M. & Munro, E.M., 2018a. Excitable RhoA dynamics drive pulsed contractions in the early C-elegans embryo. *Journal of Cell Biology*, 217(12), pp.4230–4252.

Michaux, J.B., Robin, F.B., McFadden, W.M. & Munro, E.M., 2018b. Excitable RhoA dynamics drive pulsed contractions in the early C. elegans embryo. *The Journal of Cell Biology*, 217(12), pp.4230–4252.

Miller, A.L. & Bement, W.M., 2009. Regulation of cytokinesis by Rho GTPase flux. *Nature Cell Biology*, 11(1), pp.71–77.

Munjal, A. & Lecuit, T., 2014. Actomyosin networks and tissue morphogenesis. *Development*, 141(9), pp.1789–1793. Available at: http://dev.biologists.org/cgi/doi/10.1242/dev.091645.

Munro, E., Nance, J. & Priess, J.R., 2004. Cortical flows powered by asymmetrical contraction transport PAR proteins to establish and maintain anterior-posterior polarity in the early C. elegans embryo. *Developmental Cell*, 7(3), pp.413–424.

Naganathan, S.R. et al., 2018. Morphogenetic degeneracies in the actomyosin cortex. *eLife*, 7, p.354.

Nance, J., 2003. C. elegans PAR-3 and PAR-6 are required for apicobasal asymmetries associated with cell adhesion and gastrulation. *Development*, 130(22), pp.5339–5350.

Nance, J. & Priess, J.R., 2002. Cell polarity and gastrulation in C. elegans. *Development*, 129(2), pp.387–397.

Neidt, E.M., Scott, B.J. & Kovar, D.R., 2008. Formin Differentially Utilizes Profilin Isoforms to Rapidly Assemble Actin Filaments. *The Journal of biological chemistry*, 284(1), pp.673–684. Available at: http://www.jbc.org/cgi/doi/10.1074/jbc.M804201200.

Neidt, E.M., Skau, C.T. & Kovar, D.R., 2008. The cytokinesis formins from the nematode worm and fission yeast differentially mediate actin filament assembly. *The Journal of biological chemistry*, 283(35), pp.23872–23883. Available at: http://eutils.ncbi.nlm.nih.gov/entrez/eutils/elink.fcgi?dbfrom=pubmed&id=18577519&retmode=ref&cmd=prlinks.

Nishikawa, M. et al., 2017. Controlling contractile instabilities in the actomyosin cortex. *eLife*, 6, p.058101.

Oegema, K. & Hyman, A.A., 2006. Cell division. *WormBook*, pp.1–40.

Olson, S.K. et al., 2012. Hierarchical assembly of the eggshell and permeability barrier in C. elegans. *The Journal of Cell Biology*, 198(4), pp.731–748.

Pelletier, V. et al., 2009. Microrheology of Microtubule Solutions and Actin-Microtubule Composite Networks. *Physical Review Letters*, 102(18), p.188303.

Pollard, T.D. & Wu, J.-Q., 2010. Understanding cytokinesis: lessons from fission yeast. *Nature Reviews Molecular Cell Biology*, 11(2), pp.149–155.

Pruyne, D. et al., 2002. Role of Formins in Actin Assembly: Nucleation and Barbed-End Association. *Science*, 297(5581), pp.612–615.

Reymann, A.-C. et al., 2016. Cortical flow aligns actin filaments to form a furrow. *eLife*, 5, p.e17807.

Robin, F.B. et al., 2014. Single-molecule analysis of cell surface dynamics in Caenorhabditis elegans embryos. *Nature Methods*, 11(6), pp.677–682.

Roh-Johnson, M. et al., 2012. Triggering a cell shape change by exploiting preexisting actomyosin contractions. *Science*, 335(6073), pp.1232–1235.

Swan, K.A. et al., 1998. cyk-1: a C. elegans FH gene required for a late step in embryonic cytokinesis. *Journal of Cell Science*, 111 (Pt 14), pp.2017–2027.

Timmons, L. & Fire, A., 1998. Specific interference by ingested dsRNA. *Nature*, 395(6705), pp.854–854.

Vavylonis, D. et al., 2008. Assembly Mechanism of the Contractile Ring for Cytokinesis by Fission Yeast. *Science*, 319(5859), pp.97–100.

Wollrab, V. et al., 2018. Polarity sorting drives remodeling of actin-myosin networks. *Journal of Cell Science*, 132(4), p.jcs219717.

Yamagata, K. & FitzHarris, G., 2013. 4D imaging reveals a shift in chromosome segregation dynamics during mouse pre-implantation development. *Cell cycle (Georgetown, Tex.)*, 12(1), pp.157–165.

Yu, Q. et al., 2018. Balance between Force Generation and Relaxation Leads to Pulsed Contraction of Actomyosin Networks. *Biophysical Journal*, 115(10), pp.2003–2013.

Figure 1

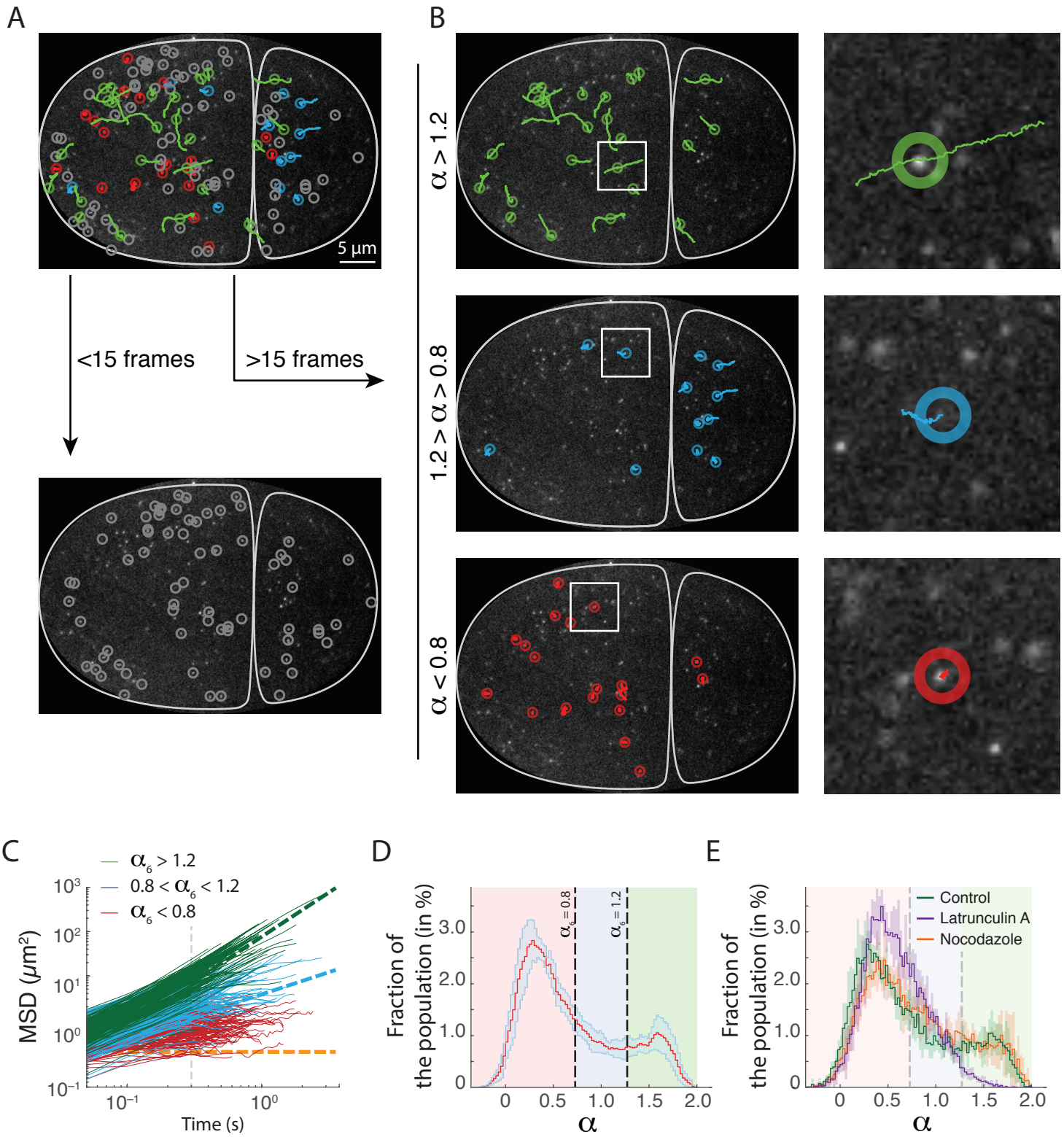
A
5 µm
<15 frames
>15 frames
B
α > 1.2
1.2 > α > 0.8
α < 0.8
C
$\alpha_6 > 1.2$
$0.8 < \alpha_6 < 1.2$
$\alpha_6 < 0.8$
MSD (µm²)
Time (s)
D
Fraction of the population (in %)
$\alpha_6 = 0.8$
$\alpha_6 = 1.2$
α
E
Control
Latrunculin A
Nocodazole
Fraction of the population (in %)
α

Figure 1. Anomalous diffusion of individual formin molecules identifies a subpopulation of actin-elongating formins. (A) Single-molecule imaging and tracking of formins shows individual behaviors ranging from superdiffusive (green) to diffusive (blue) to subdiffusive (red). **(B)** Mean-square displacement curve as a function of lag time. The slope of the curve reports on the anomalous diffusion exponent. Particles with anomalous diffusion exponent larger than 1.2 are plotted in green, between 0.8 and 1.2 in blue and smaller than 0.8 in red. Pure superdiffusive corresponds to alpha = 2 (green dashed), pure diffusive alpha = 1 (blue dashed), and immobile (orange dashed). **(C)** Distribution of the fraction of particles displaying a given anomalous diffusion exponent in 5 movies (average +/- SD). Background shows the domains corresponding to the classification used here. Two peaks seem to emerge, centered at Alpha = 0.3 and Alpha = 1.6. **(D)** Detected mobilities correspond to different classes of behaviors. Superdiffusive display a characteristic ballistic motion (green, top panel), while subdiffusive particles appear immobile in the cortex (red, bottom). **(E)** Compared to control (green curve), the superdiffusive population is absent in embryos treated with Latrunculin A (purple), but not Nocodazole (orange). More than 2000 tracks analyzed per embryo for, with >5 embryo per condition presented.

Figure 2

A

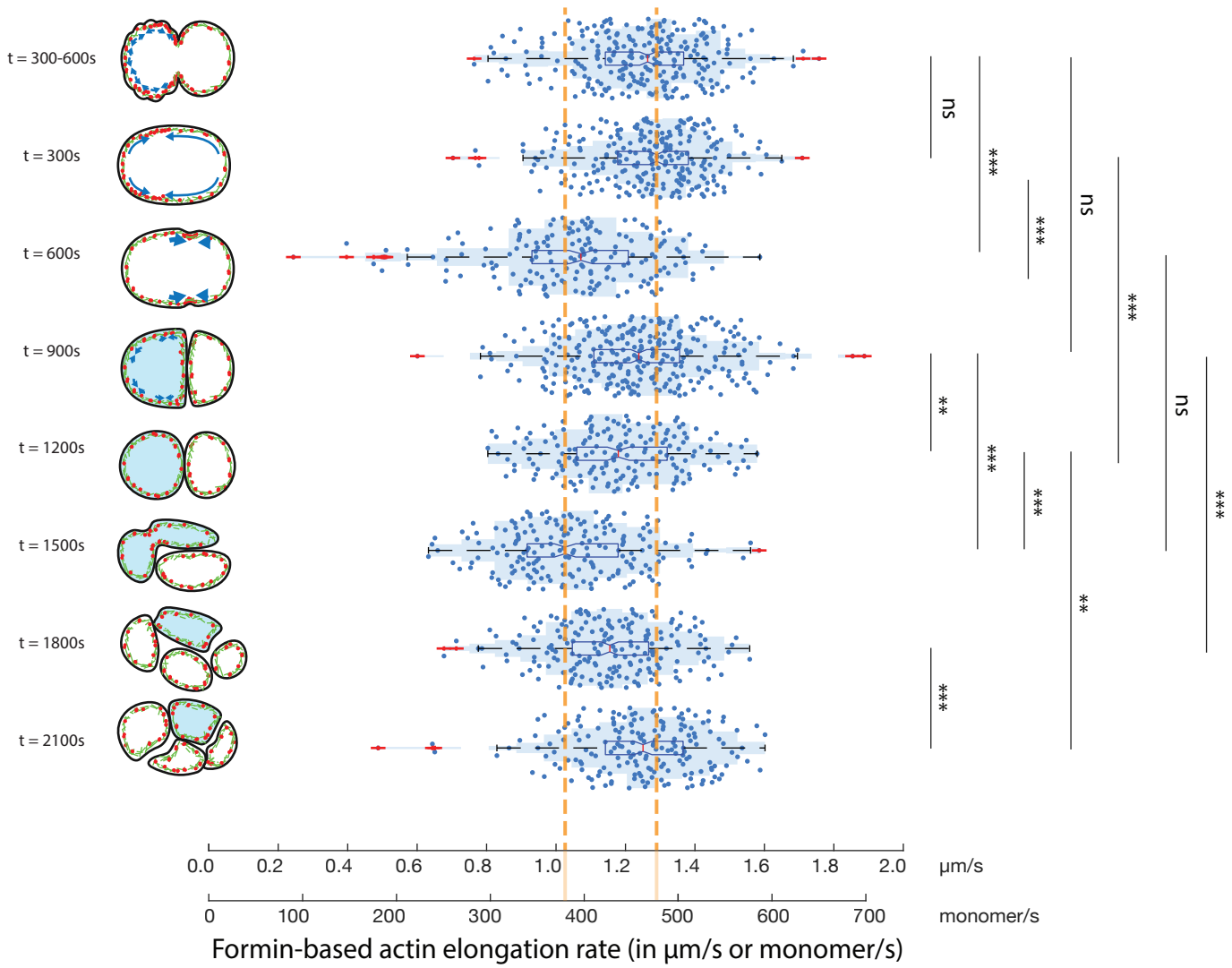
t = 300-600s
t = 300s
t = 600s
t = 900s
t = 1200s
t = 1500s
t = 1800s
t = 2100s
ns
***
***
ns
***
**
***
***
ns
**
***
0.0 0.2 0.4 0.6 0.8 1.0 1.2 1.4 1.6 1.8 2.0
µm/s
0 100 200 300 400 500 600 700
monomer/s
Formin-based actin elongation rate (in µm/s or monomer/s)

B

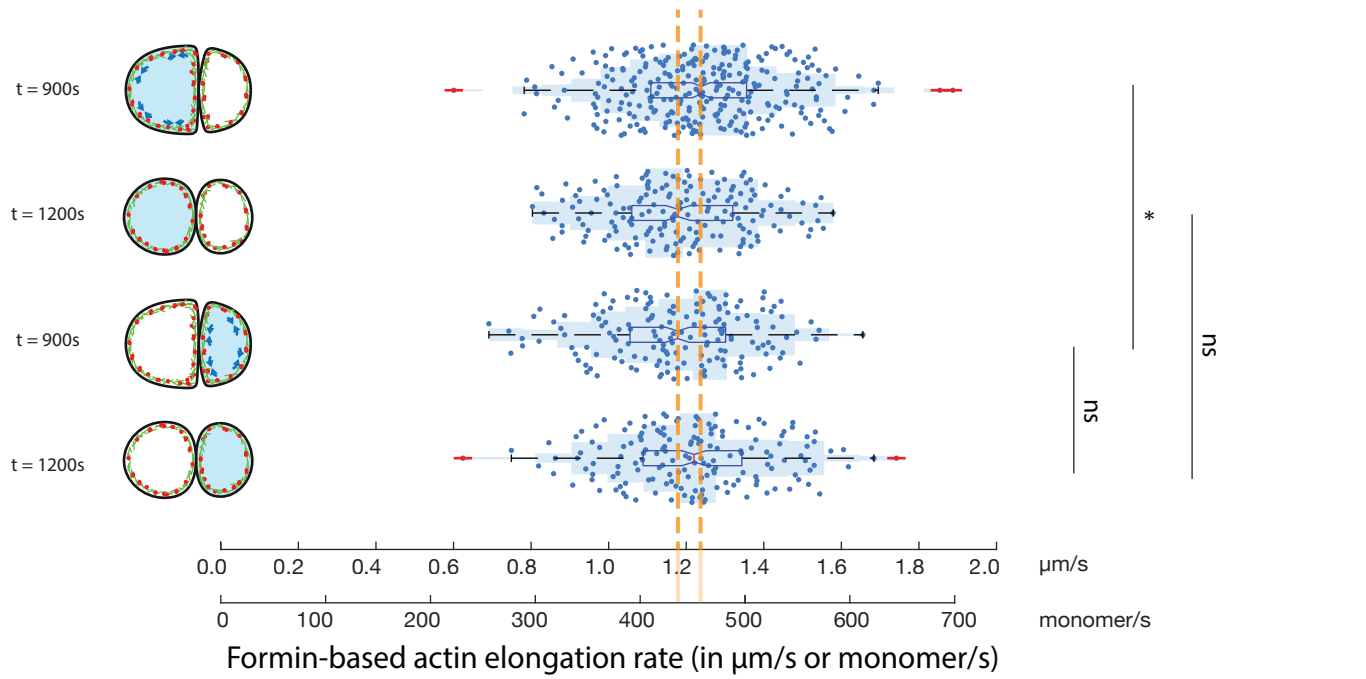
t = 900s
t = 1200s
t = 900s
t = 1200s
*
ns
ns
0.0 0.2 0.4 0.6 0.8 1.0 1.2 1.4 1.6 1.8 2.0
µm/s
0 100 200 300 400 500 600 700
monomer/s
Formin-based actin elongation rate (in µm/s or monomer/s)

Figure 2. Formin speed is changed by the cell cycle but is conserved through cell lineage. Right: Distribution of elongating Formins speed. Left: Schematic of the stage and location of the cell in which the tracks are extracted from. **(A)** Formin speed in AB cell. One-cell stage interphase: N(embryos) = 6, N(tracks) = 240 ; one-cell stage mitosis: N(embryos) = 6, N(tracks) = 240; one-cell stage cytokinesis: N(embryos) = 5, N(tracks) = 170; two-cell stage interphase: N(embryos) = 7, N(tracks) = 280; two-cell stage mitosis: N(embryos) = 7, N(tracks) = 168; two-cell cytokinesis: N(embryos) = 5, N(tracks) = 180; four-cell stage interphase: N(embryos) = 5, N(tracks) = 190; four-cell stage mitosis: N(embryos) = 5, N(tracks) = 185. Two-sample t-test on tracks: one-cell stage interphase vs one-cell stage mitosis p-value = 0,1503 ; one-cell stage interphase vs one-cell stage cytokinesis p-value = 9,92e-22 ; one-cell stage mitosis vs one-cell stage cytokinesis p-value = 1,78e-27 ; two-cell stage interphase vs two-cell stage mitosis p-value = 0,0021 ; two-cell stage interphase vs two-cell stage cytokinesis p-value = 1,12e-24 ; two-cell stage mitosis vs two-cell stage cytokinesis p-value = 2,19e-12 ; four-cell stage interphase vs four-cell stage mitosis p-value = 1,91e-06 ; one-cell stage interphase vs two-cell stage interphase p-value = 0,609 ; two-cell stage interphase vs four-cell stage interphase p-value = 6,99e-07 ; one-cell stage mitosis vs two-cell stage mitosis p-value = 3,88e-07 ; two-cell stage mitosis vs four-cell stage mitosis p-value = 0,0031 ; one-cell cytokinesis vs two-cell cytokinesis p-value = 0,8027. (B) Formin speed in P1 cell. Two-cell stage P1 interphase: N(embryos) = 7, N(tracks) = 161; two-cell stage P1 mitosis: N(embryos) = 7, N(tracks) = 161 ; two-cell stage P1 interphase vs two-cell stage P1 mitosis p-value = 0,071 ; two-cell stage AB interphase vs two-cell stage P1 interphase p-value = 0,0011 ; two-cell stage AB mitosis vs two-cell stage P1 mitosis p-value = 0,1066 (See Table S1,2 for additional statistical information).

Figure 3

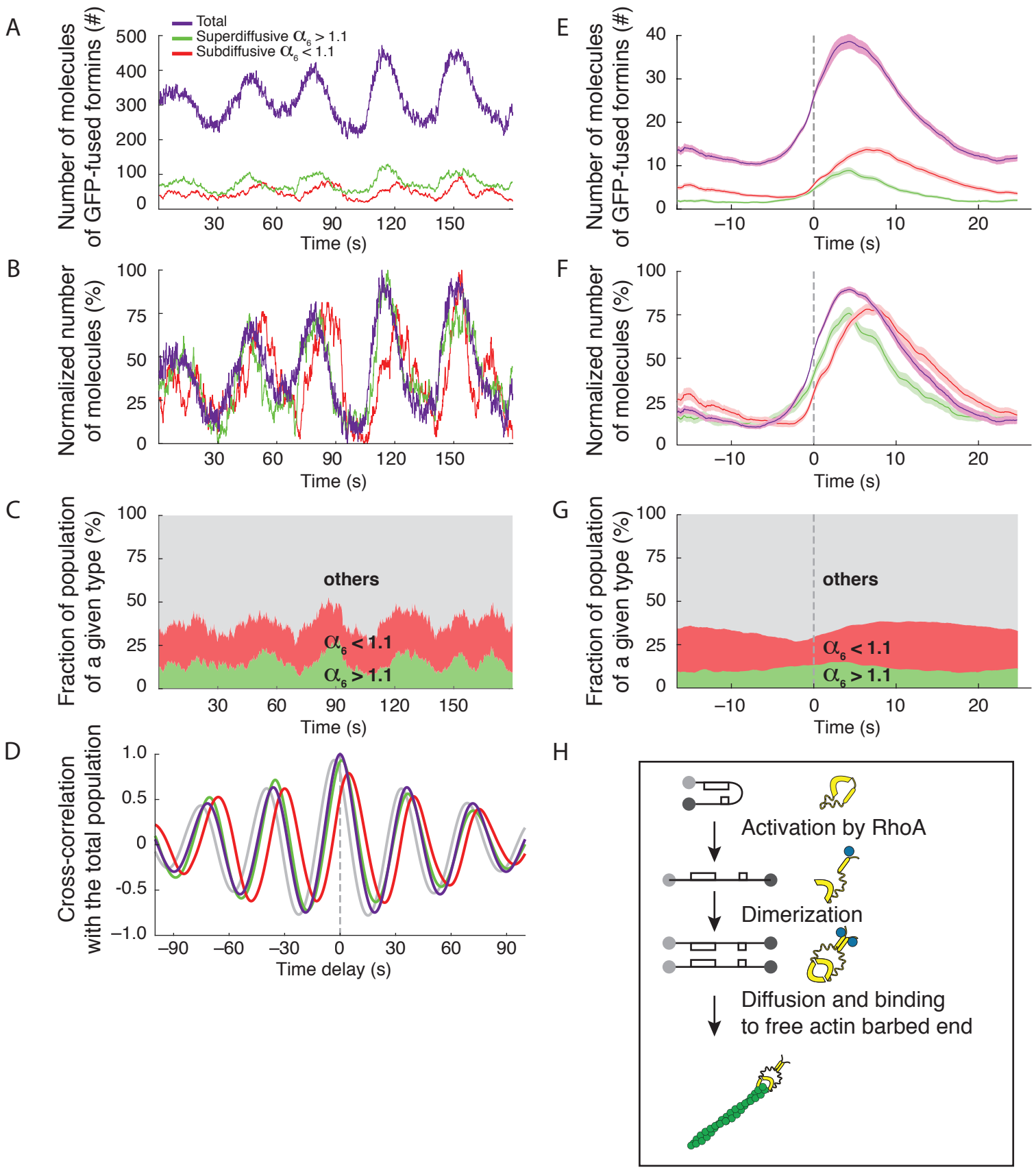
A
Total
Superdiffusive $\alpha_6 > 1.1$
Subdiffusive $\alpha_6 < 1.1$
Number of molecules of GFP-fused formins (#)
Time (s)
B
Normalized number of molecules (%)
Time (s)
C
Fraction of population of a given type (%)
others
$\alpha_6 < 1.1$
$\alpha_6 > 1.1$
Time (s)
D
Cross-correlation with the total population
Time delay (s)
E
Number of molecules of GFP-fused formins (#)
Time (s)
F
Normalized number of molecules (%)
Time (s)
G
Fraction of population of a given type (%)
others
$\alpha_6 < 1.1$
$\alpha_6 > 1.1$
Time (s)
H
Activation by RhoA
Dimerization
Diffusion and binding
to free actin barbed end

Figure 3. Inactive and active actin-elongating formins display distinct dynamics during pulsed contractions. (A-D) Analysis of GFP-fused formins molecules population dynamics in a single pulsing embryo during 5 consecutive pulsed contractions. **(A)** Number of total (purple), super-diffusive (green) and subdiffusive (red) GFP-fused formins molecules during pulsed contractions vary in a pseudo-periodic manner. **(B)** Normalized number of molecules during pulsed contractions. The populations seem to display distinct accumulation dynamics. **(C)** Temporal evolution of the relative fraction of superdiffusive (green) and subdiffusive (red) subpopulations within the total population during pulsed contractions. The relative importance of the different subpopulations varies dynamically during pulsed contractions. **(D)** Cross-correlation function of the total population with superdiffusive formins (green), subdiffusive formins (red), and other formins (grey), and with the total formin population (purple). Delays between the sub-populations appear as offset between the curves – super-diffusive and subdiffusive formins accumulate with a delay of *0.9* s and *4.6* s respectively compared with the total population, while short lived particles accumulate first, approx. 3.1s **before** the total population. The time delay between first two peaks of the autocorrelation function (purple, total population vs total population) shows that the pseudo-period of the process is approximately *36* s. **(E-K)** Analysis of GFP-fused formins molecules population dynamics in a collection of 115 individual pulses from 10 different embryos. Individual pulses are synchronized to pulse initiation (t=0), which is defined as the first pass of a threshold value of 45% of the normalized number of particles in the considered pulse (see **Fig. 5E**). **(E)** Average number of total (purple), super-diffusive (green) and subdiffusive (red) GFP-fused formins molecules during pulsed contractions. **(F)** Normalized number of molecules during pulsed contractions shows that superdiffusive, subdiffusive and total formin populations accumulate with distinct dynamics. **(G)** Average temporal evolution of the relative fraction of superdiffusive (green) and subdiffusive (red) subpopulations within the total population during individual pulsed contractions, showing that the relative importance of the different subpopulations varies dynamically during pulsed contractions. **(H)** Model of formin activation: (1) folded, auto-inhibited state, (2) RhoA binding causes unfolding, (3) unfolded formin can dimerize and (4) bind to the barbed end of, and elongate, an actin filament. Left, formin domain schematic ; right, sketch.

Figure 4

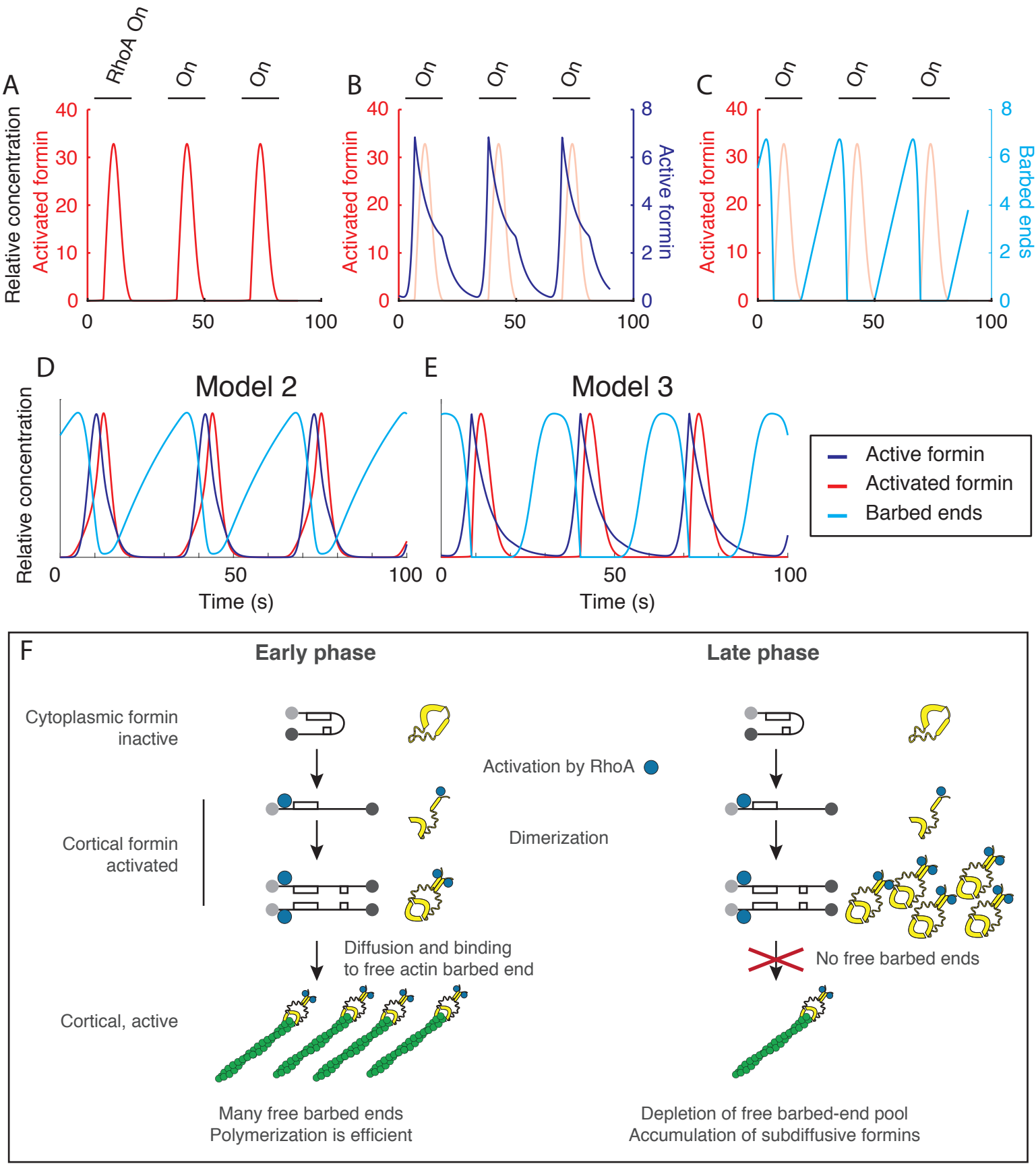
A
RhoA On
On
On
Relative concentration
Activated formin
40
30
20
10
0
0
50
100
B
On
On
On
Activated formin
Active formin
8
6
4
2
0
C
On
On
On
Activated formin
Barbed ends
D
Model 2
Relative concentration
Time (s)
E
Model 3
Time (s)
Active formin
Activated formin
Barbed ends
F
Early phase
Late phase
Cytoplasmic formin inactive
Activation by RhoA
Cortical formin activated
Dimerization
Diffusion and binding to free actin barbed end
No free barbed ends
Cortical, active
Many free barbed ends
Polymerization is efficient
Depletion of free barbed-end pool
Accumulation of subdiffusive formins

Figure 4. A mathematical model with an excess of formins with respect to the number of barbed ends results in active formins preceding activated formins. (A,B) Activated formins (red, A, washed red, B) accumulate after active formins (purple, B). **(C)** In this model, with 6 parameters, but only two free parameters, barbed ends accumulated progressively in the absence of formins (in-between pulses), but are rapidly used upon activated formins recruitment, which are immediately converted in active formins. As a result, active formins accumulate first, until depletion of the barbed end pool built up during the phase without formins. The phase during which formins are being activated, corresponding to the physiological activation of RhoA, is denoted a black line and denoted by "Rho On", or "On". **(D)** In this second model, the two free parameters of the model are modulated, resulting in a similar outcome. **(E)** In this model, barbed ends are generated periodically at the end of the pulsed contraction, representing a myosin-driven actin buckling/severing activity. Model 2 also readily reproduced the expected outcome without additional refinement. **(F)** Schematic representation of the two phases of the pulse, representing a first-come first served scenario. **Early phase:** formins arrive at the cell surface, barbed ends are available, and activated formins are immediately converted into active formins. **Late phase:** Upon depletion of the barbed end pool, formins are trapped in the activated state.

Figure 5

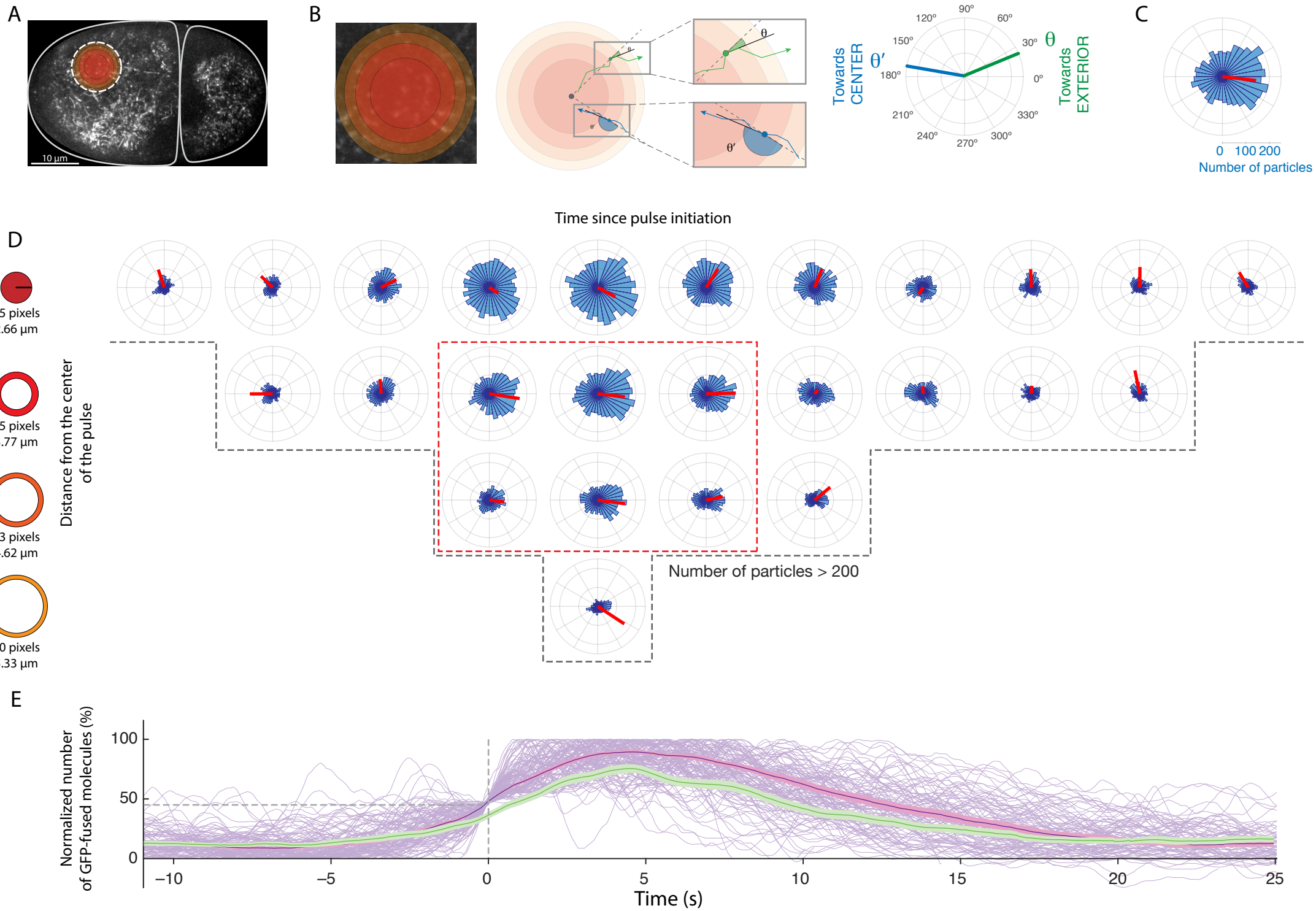
A
10 µm
B
θ
θ′
Towards CENTER
Towards EXTERIOR
90°
60°
30°
0°
330°
300°
270°
240°
210°
180°
150°
120°
C
0 100 200
Number of particles
D
Time since pulse initiation
Distance from the center of the pulse
25 pixels
2.66 µm
35 pixels
3.77 µm
43 pixels
4.62 µm
50 pixels
5.33 µm
Number of particles > 200
E
Normalized number of GFP-fused molecules (%)
100
50
0
–10
–5
0
5
10
15
20
25
Time (s)

Figure 5. CYK-1 formin-driven actin filament elongation during pulsed contractions drives the formation of a transient polar actin network, barbed ends pointing out. (A) Image of a 2-cell stage embryo labelled with CYK-1::GFP and displaying the area corresponding to a pulsed contraction (white dashed line). **(B)** Measure of the angle for two formin trajectories is performed with respect to the center of the pulse and the local orientation of the formin trajectory. The green track ($\theta \sim 25°$) is oriented with the barbed-end of the filament pointing away from the center of the pulse, while the blue track ($\theta \sim 170°$) is oriented towards the center of the pulse. **(C)** The polar histogram indicates displays the distribution of the angle measures for a large number of superdiffusive (actin-elongating) formin trajectories tracked. Average actin elongation orientation is displayed as a red segment. **(D)** Angle distribution of formin trajectories during pulsed contractions. 115 pulses derived from 10 distinct embryos were used to collect >50 000 trajectories. Trajectories are binned according to the distance from the center of the pulse (vertical) and time from t=0 (horizontal) by 3s intervals to produce each rose plot. Within a bin, trajectories are then mapped in the polar histogram according to their angle. Individual pulses are synchronized to pulse initiation (t=0), which is defined as the first pass of a threshold value of 45% of the normalized number of particles in the considered pulse (see **Fig. 5E**). Average orientation of actin elongation is calculated using circular statistics and displayed as a red segment, its length reflecting the significance of the calculated average orientation. **During the peak of the pulse around the center of the pulse, superdiffusive formins display on average an outwards orientation (dashed orange box).** Rose plots with less than 200 trajectories are considered not significant and not represented (dash line separate the region with >200 trajectories and <200). The display in (D) therefore reflects the spatio-temporal dynamics of a typical pulse. **(E)** The evolution of the number of particles in a pulse is displayed on the same axis as for D. Purple lines are synchronized, individual pulses (n=115). Dark purple curve represents corresponding average and SEM. Green curve represents average and SEM for the super-diffusive population.

Figure 6

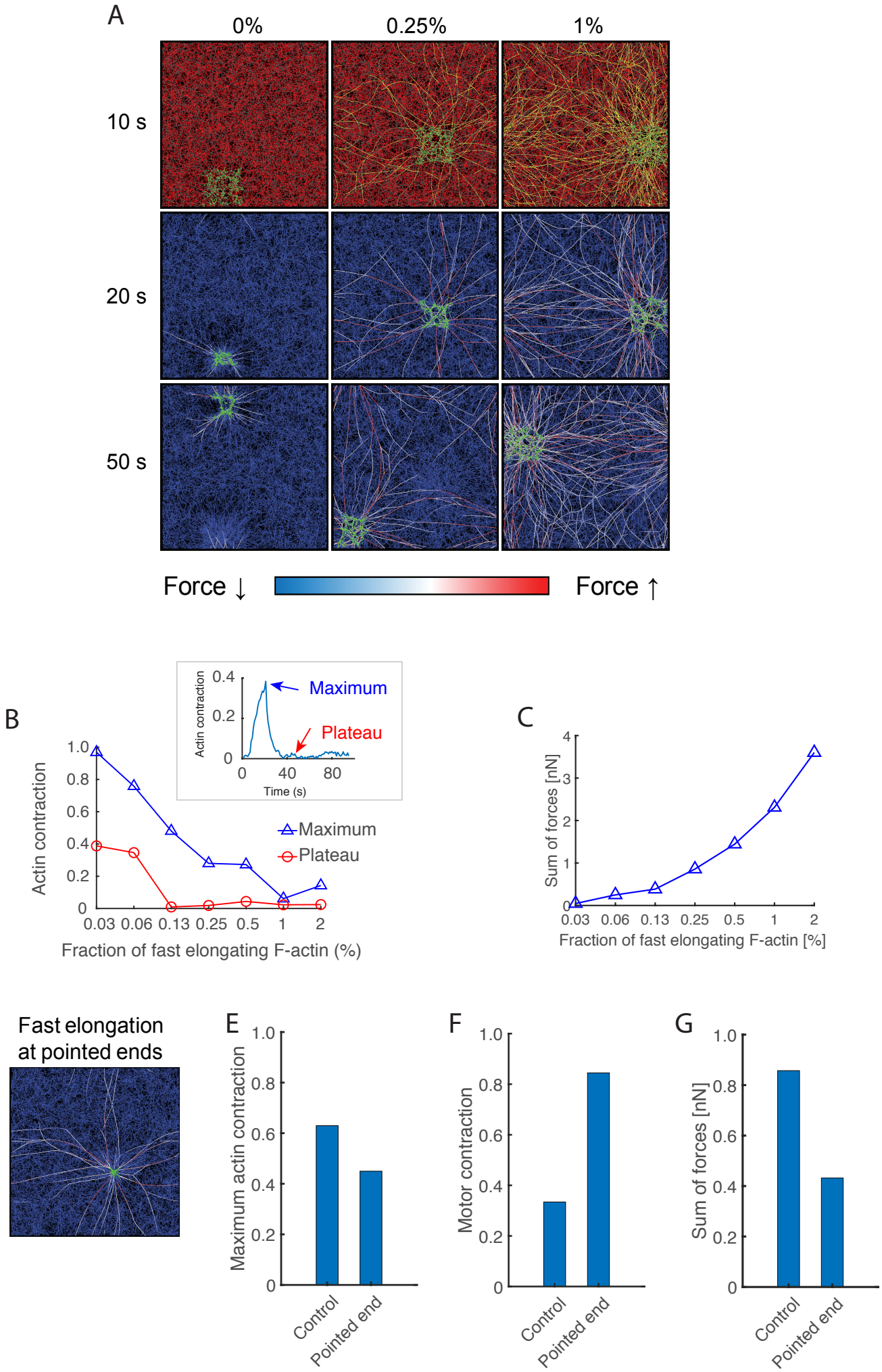
A
0%
0.25%
1%
10 s
20 s
50 s
Force ↓
Force ↑
B
Actin contraction
Maximum
Plateau
Time (s)
Fraction of fast elongating F-actin (%)
C
Sum of forces [nN]
Fraction of fast elongating F-actin [%]
D
Fast elongation at pointed ends
E
Maximum actin contraction
Control
Pointed end
F
Motor contraction
G
Sum of forces [nN]

Figure 6. Reconstruction of pulsed contraction using an agent-based computational model. (A) Snapshots taken at t = 10, 20, and 50 s with three different fractions of barbed ends undergoing quick elongation: 0%, 0.25%, and 1%. In the top row, actin, myosin, and actin cross-linking protein (ACP) are represented by red, green, and gray. Part of actin filaments elongating fast is represented by yellow. In the other rows, the magnitude of tensile forces acting on the network is visualized by color scaling shown at the bottom. Green represents active myosin motors. **(B)** The maximum (blue triangles) and plateau (red circles) values of the actin contraction as a function of the fraction of fast elongating actin filaments. Insertion top right: an example of time evolution of actin contraction measured in an activated region under a reference condition (0.25 %). **(C)** The sum of tensile forces acting on quickly elongated filaments depending on the fraction of long filaments. **(D)** Snapshot of a network with actin filaments elongated from pointed ends taken at t = 20 s. Motors still walk toward the barbed ends of actin filaments. Color schemes are identical to those applied to snapshots in the second and third rows of (A). **(E, F)** Maximum actin contraction and motor contraction quantified at t = 20 s. In the control case, filaments are elongated from barbed ends, whereas in the other case, filaments are elongated from pointed ends. **(G)** Comparison of the sum of tensile forces acting on elongated filaments between two cases. In the control case, filaments are elongated from barbed ends, whereas in the other case, filaments are elongated from pointed ends.

Figure 7

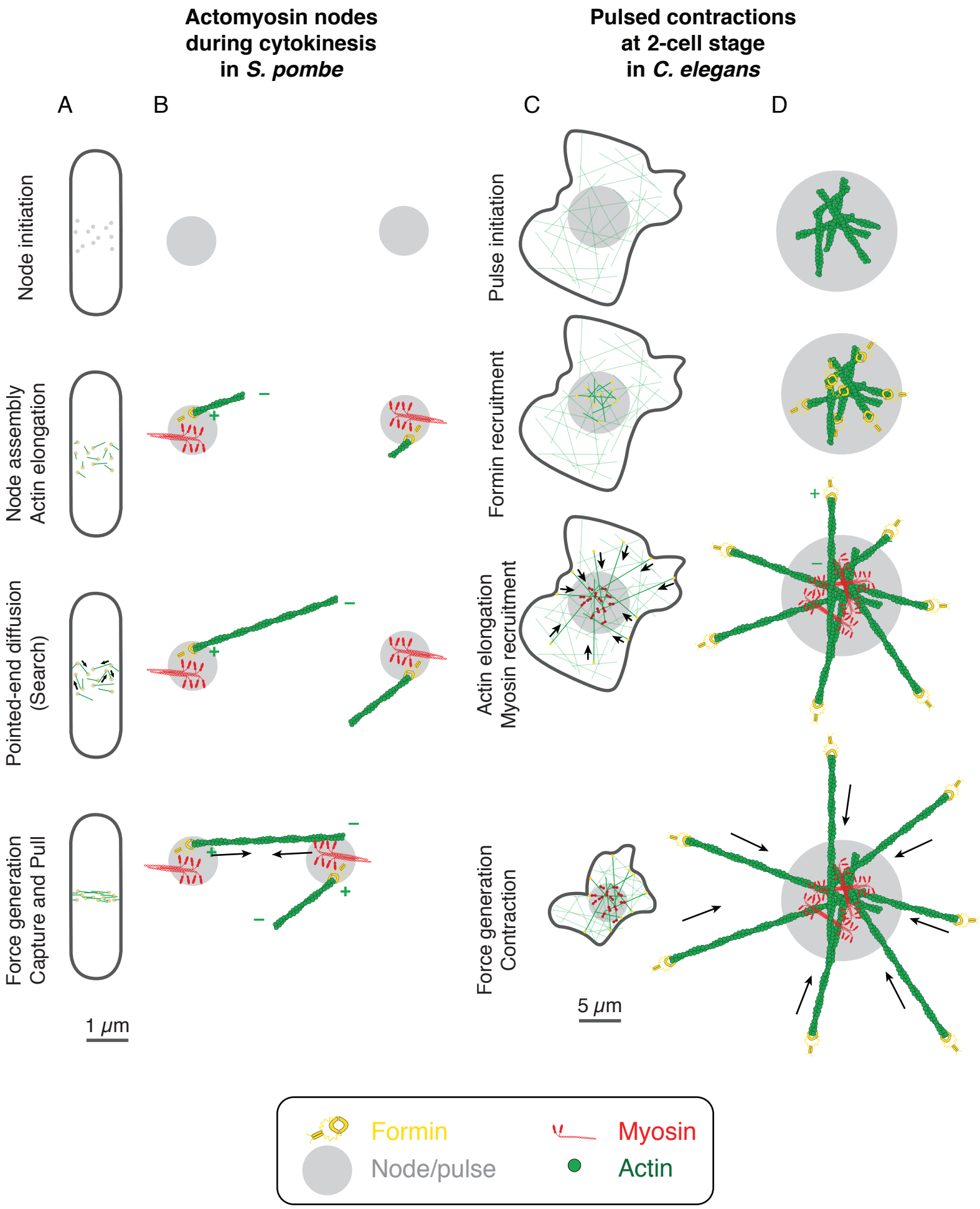
Actomyosin nodes during cytokinesis in S. pombe
Pulsed contractions at 2-cell stage in C. elegans
A
B
C
D
Node initiation
Node assembly
Actin elongation
Pointed-end diffusion
(Search)
Force generation
Capture and Pull
Pulse initiation
Formin recruitment
Actin elongation
Myosin recruitment
Force generation
Contraction
1 μm
5 μm
Formin
Node/pulse
Myosin
Actin

Figure 7. Compared analysis of contractility between pulsed contractility in metazoan (*Drosophila*, *C. elegans*) and yeast. (A) During cytokinesis in *S. pombe*, nodes form, cluster and align, forming the contractile to drive cell division, with a process scale size of 1-2 μm. Comparatively, pulsed contractions drive apical constriction (example shown) or support cleavage furrow formation in *C. elegans* (*Tse et al,* 2012) over much large distances, more along a range of 10-50 μm. **(B)** In *S. pombe*, the formin Cdc12p is recruited in the nodes and drives filament elongation. Pointed-ends of filaments are proposed to explore until they are captured and pulled by Myo2p myosin filaments of another node. **(C)** During pulsed contractions in *C. elegans,* Rho recruits formins, which will elongate actin filaments, followed by Myosin recruitment in the pulse center. Processive actin elongation by formins recruited at the pulse by Rho drives the formation of a polar actin network initiated at the pulse and extending over >10 μm from the pulse, with actin barbed-end pointing outwards. Myosin recruited by Rho in the center of the pulse then efficiently drives actin network contraction, pulling on actin cables assembled during the pulse to "reel in" the network towards the center of the pulse. Rho pulses thus convert a chemical Rho gradient in a polar actin network, with a network geometry favorable to efficient network contraction. The same machinery, but with a different topology, is used in yeast, recycling the same players to drive the same net result, contraction, but with a distinct geometry in agreement with structural constraints associated with the sizes of the two systems (*S. pombe*: 1-2 μm, *C. elegans*: 10-50 μm, actin persistence length: 1-3 μm). While extruding actin filaments is an efficient network geometry in *S. pombe*, it would likely prove ineffective in *C. elegans*, with typical pulse sizes above the actin buckling length and in a crowded cortical network.